

ACCRETION FROM A SHOCK-INFLATED COMPANION: DOUBLE-PEAKED SUPERNOVA LIGHTCURVE WITH PERIODIC MODULATIONS

WENBIN LU ¹, SAVANNAH CARY ¹ AND DAICHI TSUNA ^{2,3}

¹Department of Astronomy and Theoretical Astrophysics Center, University of California, Berkeley, CA 94720-3411, USA

²TAPIR, Mailcode 350-17, California Institute of Technology, Pasadena, CA 91125, USA and

³Research Center for the Early Universe (RESCEU), School of Science, The University of Tokyo, Bunkyo-ku, Tokyo 113-0033, Japan

Version July 22, 2025

ABSTRACT

We study the observational signatures from the interactions between a newly born neutron star and a companion star that is impacted by the supernova ejecta. We focus on the cases with bound post-explosion orbits, where the neutron star may periodically gravitationally capture gas from the companion. We find that neutron star accretion must occur if the pre-supernova binary separation is less than about $20R_{\odot}$. This is because the stellar radius expands beyond this radius before the shock-inflated envelope undergoes Kelvin-Helmholtz contraction back to the main sequence. We then consider the internal shocks formed between adjacent episodes of disk wind. The shocks efficiently convert the wind kinetic energy into radiation (due to inverse-Compton cooling), which heats up the supernova ejecta located at much larger radii. The extra heating powers bright optical emission that is periodically modulated on the orbital timescale. The shocks also accelerate non-thermal particles which produce γ -ray and neutrino emission from 100 MeV to 10 PeV via hadronic pp collisions. The high-energy photons leak out of the supernova ejecta after a delay of several months to one year. Photo-ionization of the slowest parts of the disk wind produces hydrogen recombination lines. We then use the model to explain the puzzling Type Ic supernova SN2022jli which shows a double-peaked optical lightcurve along with many peculiar properties, including delayed onset and rapid shutoff of the second peak, periodic modulations, delayed GeV emission, and narrow Balmer lines. Under this model, SN2022jli had a close companion at a pre-supernova binary separation of $10\text{--}20R_{\odot}$, likely due to an earlier phase of common-envelope evolution.

Subject headings: stars: neutron – transients – supernovae

1. INTRODUCTION

Progenitors of hydrogen-poor type Ib/c supernovae (Filippenko 1997) are believed to be dominated by intermediate-mass (~ 2.5 to $8 M_{\odot}$) helium stars whose hydrogen envelopes had been stripped by binary interaction (e.g., Podsiadlowski et al. 1992; Woosley et al. 1995; Eldridge et al. 2008, 2013; Smith et al. 2011; Drout et al. 2011; Taddia et al. 2015, 2018; Yoon 2015; Lyman et al. 2016; Prentice et al. 2019; Dessart et al. 2020; Ertl et al. 2020; Woosley et al. 2021). In this picture, the fact that roughly 20% of all core-collapse supernovae are type Ib/c explosions (e.g., Li et al. 2011; Eldridge et al. 2013; Shivvers et al. 2017) suggests that their companions are mostly main-sequence stars (e.g., Liu et al. 2015; Zapartas et al. 2017).

In such binary systems, an important effect is the impact of the supernova ejecta on the companion star. This hydrodynamic interaction has a few interesting outcomes that are well-studied in the literature (e.g., Wheeler et al. 1975; Fryxell & Arnett 1981; Marietta et al. 2000; Kasen 2010; Hirai et al. 2014; Rimoldi et al. 2016; Hirai et al. 2018; Liu et al. 2015; Ogata et al. 2021; Hober et al. 2022; Chen et al. 2023): (i) A small fraction of the companion’s mass is stripped; (ii) the shock-heated bound layers of the companion star expands to much larger radii

and the star may stay highly inflated for up to many decades after the impact; (iii) the momentum impact on the companion star may affect the orbital dynamics; (iv) the reverse shock that heats up part of the ejecta may briefly brighten up the supernova emission. These outcomes strongly depend on the mass of the companion star and the orbital separation, which are theoretically uncertain and observationally poorly constrained.

For a few type Ib/c supernovae, the post-explosion images provide potential detections or stringent upper limits on the luminosity of the companion stars (Van Dyk et al. 2016; Folatelli et al. 2016; Eldridge & Maund 2016; Maund et al. 2016; Sun et al. 2020; Fox et al. 2022). Specifically, in the case of SN2006jc, observations at 3.6 and 10.4 years after the supernova unveil a point source whose spectral energy distribution is roughly consistent with a shock-inflated companion (Maund et al. 2016; Sun et al. 2020; Ogata et al. 2021; Chen et al. 2023).

Another independent approach is to search for and study pre-explosion helium star-main sequence (He-MS) binaries in the Milky Way or nearby galaxies. Drout et al. (2023) identified a sample of 25 objects based on UV photometric excess of stars in the Large/Small Magellanic Clouds (more recently, Ludwig et al. 2025, selected a larger sample). Eight of the 25 objects appear as single-lined spectroscopic binaries with the optical spectrum

dominated by the He star (their “Class 1”). Spectroscopic modeling by [Drouot et al. \(2023\)](#) shows that the system only appears as “Class 1” if the *current* mass ratio between the MS star and He star is sufficiently small ($q \lesssim 0.6$). Since the He star’s mass is only a small fraction (roughly 1/3 for the relevant masses) of the initial mass at zero-age main sequence, [Götberg et al. \(2023\)](#) suggest that the earlier stage of Case B mass transfer that led to the stripping of the He star was dynamically unstable because of the very low accretor-to-donor mass ratio ($q \lesssim 0.2$) back then. The authors argue that a fraction of He-MS binaries are the products of common-envelope evolution, so we expect the two stars in these systems to be closely separated (the binary separation can be constrained by the not-yet-published radial velocity measurements).

Based on the mass-luminosity relation of core He burning stars, [Götberg et al. \(2023\)](#) roughly estimate the “evolutionary masses” of the He stars in the “Class 1” sample to be in the range $2 \lesssim M_{\text{He}} \lesssim 8M_{\odot}$ with a median around $3.3M_{\odot}$. Thus, it is likely that more than half of these He stars will later on produce core-collapse supernovae ([Woosley 2019](#)). Such supernovae would belong to Type Ib/c, if the remaining hydrogen-rich layer and a fraction of the helium-rich layer are further stripped by wind and mass transfer (e.g., [Tauris et al. 2015](#); [Laplace et al. 2020](#)). If there is a substantial amount of hydrogen left at explosion, then the supernova would belong to Type IIb, which is another type of stripped-envelope supernovae that we do not discuss in this paper. In those cases, the companion star may be in orbits that are too wide for the ejecta-companion interaction to be important.

Motivated by the above observations, we *assume* that a fraction of the progenitors of Type Ib/c supernovae are in close orbits with a MS companion star. For such close orbits, the newly born neutron star may remain bound to the companion star even for moderately strong natal kicks. Therefore, if the shock-heated outer layers of the companion star expands to large radii, the bound neutron star will likely strongly interact with the inflated stellar envelope. Such interactions have been predicted by [Rimoldi et al. \(2016\)](#); [Hirai et al. \(2018\)](#); [Ogata et al. \(2021\)](#); [Hober et al. \(2022\)](#). These authors briefly considered the possibility of mass transfer, neutron star accretion, orbital circularization, and formation of Thorne-Żytkow objects ([Thorne & Zytkow 1977](#)) and pulsar planets. [Hirai & Podsiadlowski \(2022\)](#) carried out hydrodynamic simulations of very close encounters between a neutron star and an *unperturbed* companion star and discussed more effects such as high-velocity ejection of the companion star, merger and tidal capture, and super-Eddington accretion onto the neutron star.

In this paper, we study in more detail the interactions between the neutron star and the shock-inflated companion star, with the goal of predicting the observational signatures of such interactions during or shortly after the supernova explosion. This is similar to the work of [Tsunai & Lu \(2025\)](#), where rarer cases of the tidal disruption of the companion star are considered. We focus

on the cases with bound¹ post-explosion orbits, where the neutron star can periodically gravitationally capture gas from the companion star’s outer envelope — as the stellar envelope expands significantly after the shock impact, these cases are much more common than tidal disruptions. Our consideration is motivated by the recent discovery of a Type Ic supernova SN2022jli ([Chen et al. 2024](#); [Moore et al. 2023](#); [Cartier et al. 2024](#)), which shows a double-peaked lightcurve along with a number of peculiar properties during the second peak such as periodic modulations, GeV emission, and narrow Balmer emission lines. It is shown that the the second peak of the lightcurve is consistent with being powered by neutron star accretion from the temporarily inflated envelope of the companion star.

This paper is organized as follows. In §2, we develop a semi-analytic formalism to study the shock-heating of the outer layers of the companion star. In §3, we follow the stellar evolution after the shock impact. In §4, we study the gas accretion onto the neutron star and the associated energy output. In §5, we consider the emission from the internal shocks formed between adjacent episodes of accretion disk wind. In §6, we apply our model to the case of SN2022jli. Finally, our results are summarized in §7. Throughout this paper, we will take the neutron star’s mass, radius, and moment of inertia to be $M_{\text{ns}} = 1.4M_{\odot}$, $R_{\text{ns}} = 12 \text{ km}$, and $I_{\text{ns}} = 1.3 \times 10^{45} \text{ g cm}^2$, respectively. We use CGS units.

2. ENTROPY JUMP DUE TO SHOCK HEATING OF THE STELLAR ENVELOPE

Let us consider an unperturbed main-sequence companion star of mass M_* and radius R_* . The unperturbed stellar density and pressure profiles are denoted as $\rho(m)$ and $P(m)$, where m is the enclosed mass coordinate. The pre-explosion orbit is assumed to be circular and the separation between the supernova progenitor and the companion star is denoted as a_0 , which is generally much larger than the stellar radius.

At the position of the star, the unperturbed supernova ejecta has density $\rho_{\text{ej}}(t)$ and velocity $v_{\text{ej}}(t)$ at time t since the explosion. The ejecta provides a ram pressure $P_{\text{ram}}(t) = \rho_{\text{ej}}v_{\text{ej}}^2$ on one side of the star. For an explosion with ejecta energy E_{ej} and mass M_{ej} , we can estimate the characteristic ejecta velocity as $v_{\text{ej}} \simeq \sqrt{2E_{\text{ej}}/M_{\text{ej}}}$, and the ejecta’s density when it reaches the star’s position is roughly given by $\rho_{\text{ej}} \simeq 3M_{\text{ej}}/(4\pi a_0^3)$. Thus, the typical ram pressure of the ejecta can be estimated as

$$P_{\text{ram}} \simeq \frac{3E_{\text{ej}}}{2\pi a_0^3} = 1.4 \times 10^{15} \frac{\text{erg}}{\text{cm}^3} E_{\text{ej},51} \left(\frac{10R_{\odot}}{a_0} \right)^3, \quad (1)$$

where $E_{\text{ej},51} = E_{\text{ej}}/10^{51} \text{ erg}$. Comparing eq. (1) with the average pressure inside the star

$$\bar{P} = \frac{GM_*^2}{4\pi R_*^4} = 8.9 \times 10^{14} \frac{\text{erg}}{\text{cm}^3} \left(\frac{M_*}{M_{\odot}} \right)^2 \left(\frac{R_{\odot}}{R_*} \right)^4, \quad (2)$$

we see that, for a companion star in a very close orbit with $a_0 \lesssim 10R_{\odot}$, the forward shock will heat up a sig-

¹ In the unbound cases, the neutron star can still capture up to $\sim 10^{-4}M_{\odot}$ ([Cary et al. 2025](#)), which can provide additional power to the supernova emission.

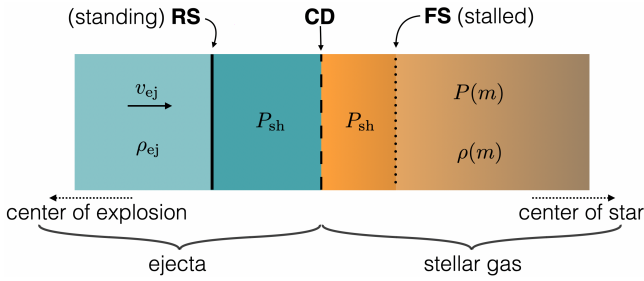


FIG. 1.— Simplified 1D *hydrostatic* configuration of the interaction between the supernova ejecta (blue regions) and the star (orange regions). In this picture, the ejecta provides a quasi-steady ram pressure $P_{\text{ram}} = \rho_{\text{ej}} v_{\text{ej}}^2$, which initially drives a forward shock (FS) into the star. As the FS propagates to a layer of mass coordinate m where the unperturbed pressure $P(m)$ is comparable to the ram pressure P_{ram} , the FS stalls and does not heat up the deeper layers. There is also a reverse shock (RS) that heats up the ejecta. Between the FS and the RS, the shock-heated ejecta and stellar gas meet each other at the contact discontinuity (CD). The pressure of the shocked region between the FS and the RS is uniform and denoted as P_{sh} .

nificant fraction of the star's mass; for wide orbits with $a_0 \gtrsim 10^2 R_\odot$, the forward shock only heats up a very small fraction of the star's mass. In this paper, we focus on the less extreme cases with $a_0 \gtrsim 10 R_\odot$.

The ram pressure varies on a timescale of

$$t_{\text{ram}} \sim \frac{a_0}{v_{\text{ej}}} = 1.2 \times 10^3 \text{ s} \frac{a_0}{10 R_\odot} E_{\text{ej},51}^{-1/2} \left(\frac{M_{\text{ej}}}{3 M_\odot} \right)^{1/2}, \quad (3)$$

where we have taken a fiducial ejecta mass for Type Ib/c supernovae. This should be compared with the shock-crossing time t_{sh} from the surface of the star to the depth where the forward shock stalls. Since the depth of the shock-heated layer is less than or equal to the stellar radius and the speed of the forward shock is greater than the local sound speed, we know that the shock-crossing time t_{sh} is generally shorter than the dynamical timescale t_* of the unperturbed star,

$$t_{\text{sh}} < t_* = \sqrt{\frac{R_*^3}{GM_*}} = 1.6 \times 10^3 \text{ s} \frac{(R_*/R_\odot)^{3/2}}{(M_*/M_\odot)^{1/2}}. \quad (4)$$

The above equations show that t_{ram} is slightly larger than but comparable to t_{sh} . This motivates us to consider the structure of the shock-heated outer layers of the star to be in quasi-hydrostatic equilibrium. Such an equilibrium is schematically shown in Fig. 1, where we have simplified the structure of the shocked gas into a one-dimensional (1D) picture.

After the forward shock sweeps past a given layer at mass coordinate m , the pressure of the shock-heated region is raised to P_{sh} , which is assumed to be roughly equal to the ram pressure P_{ram} provided by the ejecta,

$$P_{\text{sh}} \simeq P_{\text{ram}}. \quad (5)$$

The Mach number of the upstream gas in the frame of the forward shock as it passes mass coordinate m is given by (from the Rankine-Hugoniot jump conditions)

$$\mathcal{M}^2(m) = 1 + \frac{\gamma + 1}{2\gamma} \left[\frac{P_{\text{sh}}}{P(m)} - 1 \right], \quad (6)$$

where $\gamma = 5/3$ is the adiabatic index. Hereafter, we assume that gas pressure dominates over radiation pressure in the shocked stellar gas, which is true in the deeper layers where most of the energy associated with the shock heating is deposited, even though radiation pressure may become important in the outermost shock-heated layers of the star (where only a negligible fraction of the heat is deposited).

The density and temperature of the shock-heated stellar gas are given by

$$\frac{\rho_{\text{sh}}(m)}{\rho(m)} = \frac{(\gamma + 1)\mathcal{M}^2}{(\gamma - 1)\mathcal{M}^2 + 2} = \frac{4P_{\text{sh}}/P + 1}{4 + P_{\text{sh}}/P}, \quad (7)$$

and

$$T_{\text{sh}}(m) = \frac{\mu m_{\text{p}} P_{\text{sh}}}{k_{\text{B}} \rho_{\text{sh}}(m)}, \quad (8)$$

where k_{B} is the Boltzmann constant and $\mu \approx 0.6$ is the mean molecular weight for solar composition.

For a non-relativistic Maxwell-Boltzmann gas that is a mixture of $i = 1, 2, \dots$ species at the same temperature T , the entropy per particle s_i for each species with number density n_i and particle mass m_i is given by

$$\frac{s_i}{k_{\text{B}}} = \frac{5}{2} + \ln \left[\frac{g_i}{n_i} \left(\frac{2\pi m_i k_{\text{B}} T}{h^2} \right)^{3/2} \right], \quad (9)$$

where g_i is the statistical weight: $g_i = 2$ for protons and electrons (spin 1/2 particles) whereas $g_i = 1$ for helium nuclei (spin 0). The total entropy per unit mass (or specific entropy) of the gas mixture is given by

$$s = \frac{\sum_i n_i s_i}{\rho}. \quad (10)$$

As long as the gas composition stays unchanged across the shock front, the specific entropy has the following dependences on pressure and density:

$$s = \frac{3k_{\text{B}}}{2\mu m_{\text{p}}} \ln(P/\rho^{5/3}) + \text{const}. \quad (11)$$

Based on eqs. (11) and (7), we can calculate the entropy jump due to the heating by the forward shock $\Delta s(m) = s_{\text{sh}} - s$, where $s(m)$ and $s_{\text{sh}}(m)$ are the entropies for the unperturbed and shock-heated gas at mass coordinate m , respectively. The result is

$$\begin{aligned} \Delta s(m) &= \frac{k_{\text{B}}}{\mu m_{\text{p}}} \left[\frac{3}{2} \ln \frac{P_{\text{sh}}}{P(m)} - \frac{5}{2} \ln \frac{\rho_{\text{sh}}}{\rho(m)} \right] \\ &= \frac{3k_{\text{B}}}{2\mu m_{\text{p}}} \ln \left[x \left(\frac{4+x}{1+4x} \right)^{5/3} \right], \quad x \equiv \frac{P_{\text{sh}}}{P(m)}. \end{aligned} \quad (12)$$

If the ram pressure is much smaller than the central pressure of the star, then there is a minimum mass coordinate m_{min} at which $\Delta s(m_{\text{min}}) = 0$ and $P_{\text{sh}} = P(m_{\text{min}})$. This mass coordinate is where the forward shock stalls. If the ram pressure is higher than the central pressure of the star, then the entire star will be shock heated in our quasi-static picture.

The pressure profile is the simplest for the outermost layers of the star where the enclosed mass is $m \approx M_*$ (and $r \approx R_*$). Based on the equation of hydrostatic equilibrium (assuming a non-rotating star),

$$\frac{dP}{dr} = -\frac{Gm(r)}{r^2}\rho = -\frac{Gm(r)}{r^2}\frac{dm}{4\pi r^2 dr}, \quad (13)$$

we take $r \approx R_*$ and $m \approx M_*$ and obtain

$$dP \approx \frac{GM_*}{4\pi R_*^4} dm. \quad (14)$$

This means that the pressure is related to the enclosed mass m via

$$P(m) \approx \bar{P}(1 - m/M_*), \quad \text{for } m \approx M_*, \quad (15)$$

where \bar{P} is given by eq. (2). After the passage of the forward shock, the pressure jump at mass coordinate m is given by

$$x(m) = \frac{P_{\text{sh}}}{P(m)} \approx \frac{P_{\text{sh}}}{\bar{P}} \frac{M_*}{M_* - m}, \quad (16)$$

which can then be plugged into eq. (12) to obtain the entropy jump. In the limit of $x \gg 1$ near the stellar surface, the entropy jump is given by

$$\Delta s(m) \approx \frac{3k_{\text{B}}}{2\mu m_{\text{p}}} \ln \left[\frac{P_{\text{sh}}}{4^{5/3} \bar{P}} \frac{M_*}{M_* - m} \right], \quad \text{for } m \approx M_*. \quad (17)$$

We see that the entropy jump has the following scaling $e^{\Delta s(m)} \propto (M_* - m)^{-1}$, which is in agreement with the results from numerical simulations by Hirai et al. (2018, see their Fig. 18). Our analytical theory also predicts that the entropy jump diverges logarithmically near the surface of the star where $m/M_* \rightarrow 1$. This divergence is unphysical because (i) the layers very close to the stellar surface will be rapidly stripped away from the star (hydrostatic equilibrium is not possible), and (ii) the surface layers at sufficiently small optical depth can radiatively cool. In the Appendix, we show that this divergence is unimportant for the subsequent evolution of the ejecta-impacted companion star, because most of the shock-generated heat is deposited near the deepest layer where the forward shock stalls.

In our 1D hydrostatic picture, we assume $P_{\text{sh}} \simeq P_{\text{ram}}$. However, realistic systems are different from our simplified picture because (i) both the forward and reverse shocks are generally oblique mainly due to the curvature of the stellar surface and (ii) the shocked gas can escape sideways which will reduce P_{sh} as compared to the 1D hydrostatic case. Therefore, the exact ratio of $P_{\text{sh}}/P_{\text{ram}}$ needs to be calibrated against numerical simulations in future works for the purpose of making more accurate observational predictions.

Apart from the 1D simplification, another shortcoming of our analytic model is the ignorance of mass loss from the companion star. It is well-known that the ejecta's impact causes the highest entropy surface layers of the star to become unbound to the star (Wheeler et al. 1975). This would lead to the flattening of the entropy profile of the bound layers at very small exterior masses. This flattening is not captured in our analytic model. However, the

flattening of the entropy profile makes very little practical difference in the late-time evolution of the star for the following reason. Most of the shock heating associated with the entropy jump is deposited near the bottom of the shocked stellar envelope where $P(m) \sim P_{\text{sh}}$. Only a very small fraction of the heat is deposited to the surface layers that escape from the star and this amount of heat is quickly radiated away in the subsequent evolution of the shock-heated star. The unimportance of the entropy profile flattening is demonstrated in the Appendix (see Fig. 17). Since the fractional mass loss is a steeply decreasing function of the separation between the two stars (e.g., Hirai et al. 2018), we expect our analytic model to work best for relatively large binary separations.

In the next section, we take the entropy jump given by our analytic model (eq. 12) as the initial conditions to study the subsequent evolution of the shock-heated stars.

3. EVOLUTION OF SHOCK-HEATED STARS

In this section, we use Modules for Experiments in Stellar Astrophysics (MESA, Paxton et al. 2011, 2013, 2015, 2018, 2019; Jermyn et al. 2023) to study the long-term evolution of the shock-heated companion star. We apply the model to a large grid of parameters (M_*, a_0) that would be more computationally expensive for detailed multi-dimensional numerical simulations to cover. Our method, which follows the work by Bauer et al. (2019) (see also Pan et al. 2012), is described in §3.1, and our results are presented in §3.2.

3.1. Method

The initial condition is a zero-age main-sequence star of a given mass M_* at solar metallicity. To capture the effect of the ejecta's impact, we model the entropy jump as given by eq. (12) at each mass coordinate m by heat injection at a rate $\dot{q}(m, t)$ (heating rate per unit mass) such that

$$\Delta s(m) = \int_0^{\Delta t} \frac{\dot{q}(m, t)}{T(m, t)} dt, \quad (18)$$

where Δt is the heating duration and $T(m, t)$ is the current temperature profile at time t since the beginning of heating. We pick a global duration Δt and then adopt a steady entropy injection rate

$$\dot{s}(m) = \Delta s(m)/\Delta t, \quad (19)$$

which is applied to each Lagrangian layer as labeled by its mass coordinate m . Note that the heating rate at a given time is adjusted according to the current temperature $T(m, t)$ such that it produces the desired constant entropy injection rate $\dot{s}(m)$. At $t > \Delta t$ since the beginning of heating, we turn off heating and continue to evolve the star for a maximum age of 10^4 yr by which time the star has returned to the main-sequence. In all our simulations, we fix $\Delta t = 10^4$ s (roughly 0.1 d), as our results are insensitive to Δt as long as it is much shorter than the thermal expansion timescale of the envelope (this is tested in the Appendix).

To avoid the logarithmic divergence of the entropy jump near the stellar surface, we consider a minimum *exterior* mass $m_{\text{ex, min}}$ below which the entropy jump is assumed

to be flat, meaning that

$$\Delta s(m > M_* - m_{\text{ex,min}}) = \Delta s(m = M_* - m_{\text{ex,min}}). \quad (20)$$

In all our simulations, we fix $m_{\text{ex,min}} = 10^{-5}M_\odot$ and the evolution of the shock-heated star is insensitive to our choice of $m_{\text{ex,min}}$ as long as it is much smaller than the total mass of the shock-heated layers (this is tested in the Appendix).

In our model, the ejecta energy E_{ej} is degenerate with the pre-explosion orbital separation a_0 through the ram pressure in eq. (1), so we fix $E_{\text{ej}} = 10^{51}$ erg as is typical for Type Ib/c supernovae (e.g., Lyman et al. 2016).

Then, we are left with two free parameters, the companion mass M_* and pre-explosion orbital separation a_0 . For a given supernova, these two parameters are practically unconstrained from the standard supernova emission alone. Our goal is to demonstrate that, if the newly born neutron star accretes from the inflated companion star, the radiative signature of the accretion power can in principle be used to constrain M_* and a_0 . However, as we will show later, it turns out that only a_0 is strongly constrained.

In the following, we take a logarithmic grid in both dimensions:

$$M_*/M_\odot = 1.3, 2.0, 3.0, 4.5, 6.7, 10.0, \quad (21)$$

and

$$a_0/R_\odot = 12, 18, 27, 40, 60. \quad (22)$$

In our model, the a_0 's above correspond to the pressures of the shock-heated gas $P_{\text{sh}} = P_{\text{ram}}$ as

$$\log \frac{P_{\text{sh}}}{\text{erg cm}^{-3}} = 14.9, 14.4, 13.9, 13.3, 12.8. \quad (23)$$

Our method likely becomes less accurate at smaller orbital separations $a_0 \lesssim 10R_\odot$, because (i) the mass stripping by the ejecta's impact becomes significant, (ii) the forward shock directly passes through a large fraction of the star's volume which causes our 1D approximation to break down.

3.2. Results

To illustrate the long-term evolution of the shock-heated star, we will focus on two representative examples with $M_* = 2M_\odot$ and $10M_\odot$ and then present the metadata for other stellar masses.

The evolution of stellar radius and on the Hertzsprung-Russell (HR) diagram for the cases with $M_* = 2M_\odot$ and $10M_\odot$ are shown in Figs. 2–5. We find that the star expands to large radii: for the strongest impact considered in our grid of models, the radii grows up to 10^2R_\odot , which is driven by hydrodynamic pressure adjustment of the outer layers. It takes up to about one year for the star to expand to the maximum radius. Subsequently, the star undergoes Kelvin-Helmholtz contraction as the shock-injected energy is radiated away. During the expansion and contraction, the star stays significantly brighter than the initial main-sequence state for an extended amount of time, ranging from decades to millennia, depending on the pre-supernova separation. These results are very similar to those found by Chen et al. (2023) (see, e.g.,

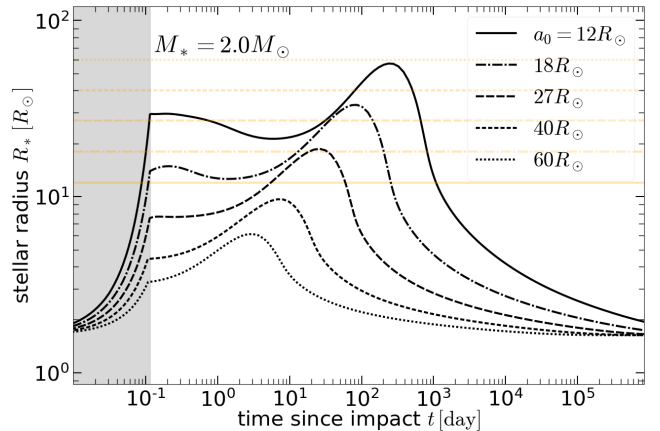


FIG. 2.— Radius evolution (black lines) after the ejecta's impact for a $M_* = 2M_\odot$ main-sequence companion star placed at different pre-supernova orbital separations a_0 (as shown by the horizontal orange lines). The grey region at $t < 10^4$ s marks the heat-injection episode which mimics the entropy jump due to shock-heating.

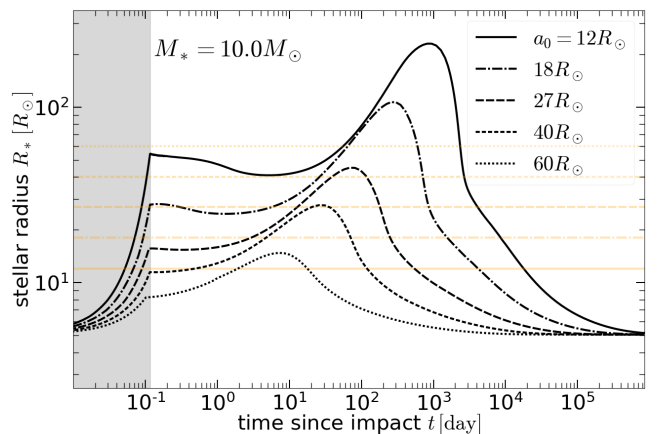


FIG. 3.— Same as Fig. 2, but for $M_* = 10M_\odot$.

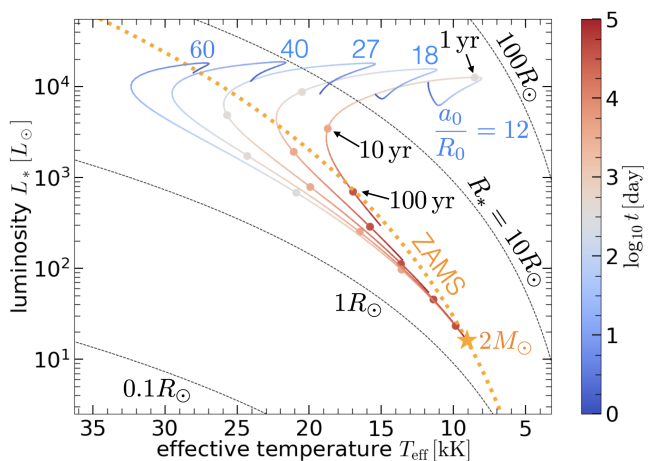


FIG. 4.— Evolution of an ejecta-impacted $M_* = 2M_\odot$ main-sequence star on the HR diagram. The colored lines correspond to different pre-supernova orbital separations a_0 . Along each line, three filled circles indicate different times since the impact $t = 1, 10, 100$ yr. The black dotted lines show different stellar radii $R_* = 0.1, 1, 10, 100R_\odot$. The thick orange dotted line marks the main sequence, and the orange star represents the initial condition of the companion star.

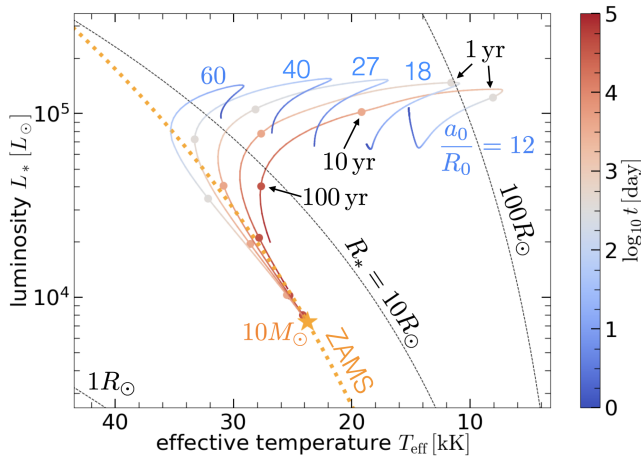


FIG. 5.— Same as Fig. 4, but for $M_* = 10M_\odot$.

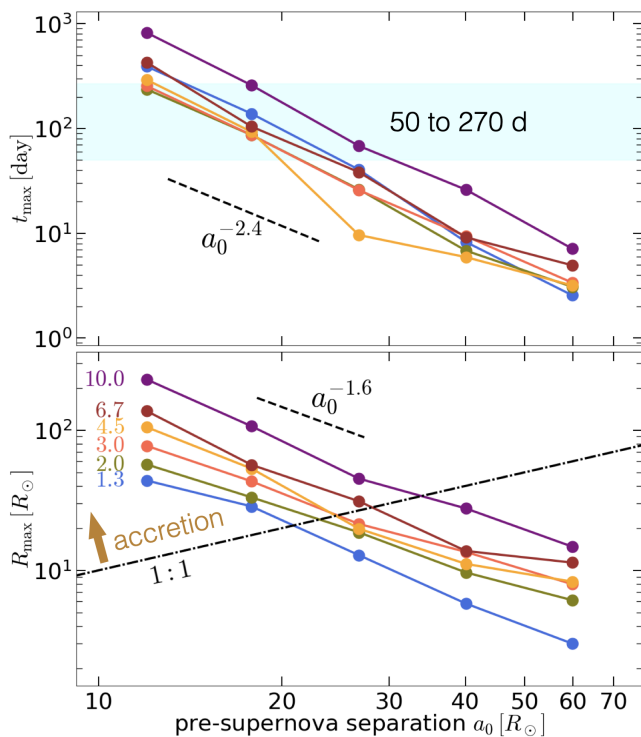


FIG. 6.— The maximum radius R_{\max} (lower panel) and the time to reach the maximum radius t_{\max} (upper panel) for each of the models. In the upper panel, the cyan region marks the time between $t = 50$ and 270 day when the inferred energy injection occurs in SN2022jli (Chen et al. 2024). In the lower panel, the black dashed-dotted line shows $R_{\max} = a_0$ above which a neutron star bound to the companion must accrete, as the post-supernova orbital pericenter radius is always less than a_0 .

their Fig. 7), who comprehensively discussed the observability of the shock-heated star using different optical filters.

Below, we provide a qualitative explanation of the radius expansion of the shock-heated star. Let us denote the maximum radius as R_{\max} and the time to reach the maximum radius as t_{\max} .

Based on the dynamical timescale of the maximally inflated star, we roughly expect $t_{\max} \propto R_{\max}^{3/2} M_*^{-1/2}$. On the other hand, t_{\max} should also be roughly

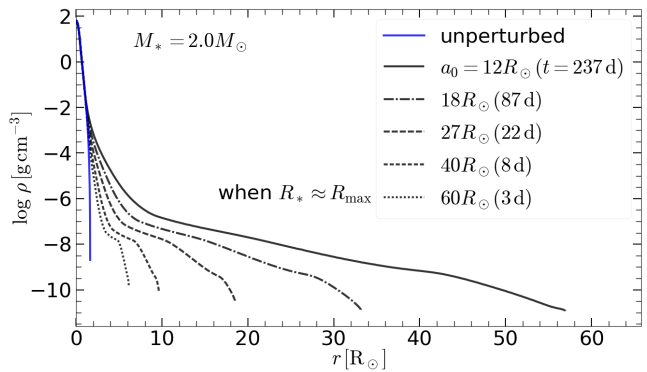


FIG. 7.— Black lines show the density profiles of the $M_* = 2M_\odot$ star near maximum radius ($R_* \approx R_{\max}$) for different pre-supernova orbital separations a_0 . The blue solid line shows the unperturbed density profile.

equal to the Kelvin-Helmholtz cooling timescale of the inflated envelope, and this means that $t_{\max} \sim GM_* M_{\text{sh}} / (R_{\max} L_{\text{Edd},*})$, where $M_{\text{sh}} \propto M_* P_{\text{sh}} / P$ is the mass of the shock-heated layer (eq. 17). We have taken the maximum luminosity to be of the order the star’s Eddington luminosity $L_{\text{Edd},*} \propto M_*$ (assuming a constant opacity). From the mass-radius relation of the unperturbed stars $R_* \propto M_*^{\approx 0.5}$ as given by our MESA models, we see that the average pressures of the stars \bar{P} (eq. 2) are nearly independent of the masses. We then put the dynamical and cooling timescales together and find that $R_{\max} \propto a_0^{-6/5} M_*^{3/5}$ and $t_{\max} \propto a_0^{-9/5} M_*^{2/5}$, where we have used $P_{\text{sh}} \propto a_0^{-3}$ for a constant explosion energy.

The above scalings are only approximate, as the detailed evolution is more complicated than the analytic estimates. Our numerical results (shown in Fig. 6) can be well described by the following empirical relations

$$R_{\max} \simeq 70 R_\odot (a_0/10R_\odot)^{-8/5} (M_*/2M_\odot)^{1/3}, \quad (24)$$

and

$$t_{\max} \simeq 290 \text{ d } (a_0/10R_\odot)^{-12/5}. \quad (25)$$

In the following, we focus on the properties of the inflated star that are relevant for the accretion onto the neutron star under the assumption that the binary system remains bound after the supernova.

Fig. 7 shows the density profiles of the shock-inflated $M_* = 2M_\odot$ star near the maximum radius $R_* \approx R_{\max}$ for five different pre-supernova orbital separations a_0 . In §4, we will use the time-dependent density and pressure profiles to calculate the amount of gas that will be gravitationally captured by the neutron star as well as the corresponding accretion power.

For a given post-supernova orbit (which is mainly determined by the ejecta mass and the neutron star’s natal kick), accretion onto the neutron star starts when the radius of the companion star R_* exceeds the orbital pericenter radius r_p . The accretion rate is the highest when the companion star reaches the maximum radius R_{\max} . From Fig. 2, we see the maximum accretion rate is achieved after a significant delay of up to about one year (depending on the pre-supernova orbital separation) af-

ter the supernova explosion. Since the radioactive decay-powered emission in a typical Type Ib/c supernova usually peaks within a few weeks after the explosion, the delay in post-supernova accretion makes it possible to form a second peak in the observed lightcurve — this is a unique feature of our model.

In the literature, there are two other well-studied mechanisms for late-time energy injection from a compact object: (i) the magnetic dipole spin-down power from the neutron star (Kasen & Bildsten 2010; Woosley 2010; Metzger et al. 2015), and (ii) fallback accretion of the marginally bound ejecta (e.g., Dexter & Kasen 2013; Kashiwama & Quataert 2015; Metzger et al. 2018). These two mechanisms do not predict a second peak with a significant delay, because the energy injection is “on” at a very early time² since the explosion. Another possible mechanism that can power late-time emission is the interaction between the supernova ejecta with the circumstellar medium (e.g., Chatzopoulos et al. 2013; Dessart et al. 2015a; Khatami & Kasen 2023). The special case of a detached shell of circum-stellar medium can reproduce the lightcurves of some supernovae with two peaks that are clearly separated (Tsunai & Takei 2023), but the lightcurve and spectroscopic signatures will be different from those in our model where the heating source is located inside the supernova ejecta and the accretion power is modulated by orbital motion (see §6).

Interactions between the neutron star and companion star must occur if $R_{\max} > a_0$ because the post-explosion orbital pericenter radius satisfies $r_p \leq a_0$. Thus, we obtain the following *sufficient* condition for accretion:

$$R_{\max}(a_0) > a_0 \Rightarrow a_0 \lesssim 20R_{\odot}(M_*/2M_{\odot})^{0.1}, \quad (26)$$

which depends weakly on the companion mass.

4. NEUTRON STAR ACCRETION

In this section, we assume that the newly born neutron star remains bound to the companion star (see §6.1 for the conditions) and study the interactions between the neutron star and the shock-inflated companion star. We first estimate the mass captured by the neutron star’s gravitational potential in each orbit (§4.1) and then consider the power generated by accretion (§4.2).

4.1. Bondi-Hoyle-Lyttleton mass capture

Below, we estimate the rate of Bondi-Hoyle-Lyttleton mass capture (hereafter “Bondi capture”) by the neutron star if its orbit goes through the companion star’s inflated envelope. Let us denote the post-supernova orbital pericenter separation as r_p and semimajor axis as a . The orbital velocity v (relative velocity between the two stars) at a given separation r is given by

$$v(r) = \sqrt{G(M_{\text{ns}} + M_*)(2/r - 1/a)}, \quad (27)$$

where M_{ns} is the neutron star’s mass. The critical impact parameter within which gas becomes gravitationally bound to the neutron star is given by the Bondi radius

² Unless the magnetic dipole moment of the neutron star is enhanced in an unexpected way many weeks after the supernova (see e.g., Chugai & Utrobin 2022).

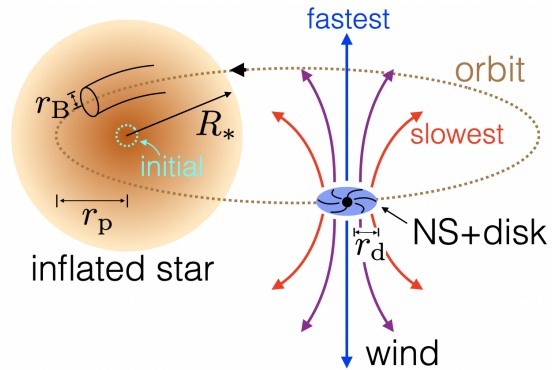


FIG. 8.— Geometry of the post-supernova binary system.

(Edgar 2004)

$$r_B(r) = \frac{2GM_{\text{ns}}}{v^2 + c_s^2}, \quad (28)$$

where c_s is the adiabatic sound speed of the surrounding gas, and we have ignored the companion star’s gravitational potential as the Hill radius of the neutron star $r_H = r(M_{\text{ns}}/M_*)^{1/3}$ (within which the neutron star’s gravity dominates over that of the companion) is usually much greater than r_B .

Another important quantity is the density scale height of the stellar envelope

$$H_\rho(r) \equiv |d \ln \rho / dr|^{-1}. \quad (29)$$

This is related to the pressure scale height

$$H_P(r) \equiv |d \ln P / dr|^{-1} \approx \frac{P}{\rho} \frac{r^2}{GM_*} = \frac{c_s^2 r^2}{\gamma GM_*}, \quad (30)$$

where $\gamma \approx 5/3$ is the adiabatic index of the gas. We assume quasi-hydrostatic equilibrium in the envelope, and we have taken $m(r) \approx M_*$ as the envelope only contains a small fraction of the star’s mass. These two scale heights are related to each other by

$$\frac{H_\rho}{H_P} = \frac{d \ln P}{d \ln \rho} \equiv \Gamma, \quad (31)$$

where Γ is a factor of order unity that depends on the pressure and density profiles of the envelope. In the following, we adopt³ $\Gamma \simeq 1.5$ and hence

$$H_\rho \simeq 1.5H_P, \quad (32)$$

where the factor of 1.5 comes from our numerical tests and is appropriate for regions deep inside the inflated envelope at radii of the order $10R_{\odot}$ (where efficient Bondi capture onto the neutron star occurs).

The ratio between the density scale-height and the Bondi radius is roughly given by

$$\frac{H_\rho}{r_B} \simeq \frac{c_s^2}{v^2} \frac{2\Gamma(1 + c_s^2/v^2)}{\gamma} \frac{(M_{\text{ns}} + M_*)^2}{M_{\text{ns}}M_*}, \quad (33)$$

³ Unfortunately, $d \ln P / d \ln \rho$ is a derived quantity in MESA that is only correct to the first order of the radial grid spacing, so it has significant numerical fluctuations near the stellar surface. The pressure scale height H_P is quantity that is correct to a higher order and directly saved in MESA output files, our model relies on $H_P(r)$ and a constant, empirical Γ .

where we have used a rough estimate of $v \simeq \sqrt{2G(M_{\text{ns}} + M_*)/r}$ as the typical orbital speed of the neutron star near the pericenter (where most mass is captured). Since the neutron star is moving supersonically through the envelope ($c_s \ll v$), the density scale-height H_ρ is typically less than the Bondi radius r_B . This means that density profile across the “Bondi cylinder” of radius r_B is inhomogeneous. The side closer to the stellar center has higher density than the farther side. Therefore, only the fluid elements with impact parameters $\lesssim H_\rho$ will undergo strong shock interactions and could further fall into the gravitational potential of the neutron star. The trajectories of the fluid elements with impact parameters in between H_ρ and r_B are significantly deflected by the neutron star’s gravity, but they largely maintain hyperbolic orbits and stay unbound to the neutron star during the encounter. Such a system has been numerically studied by MacLeod & Ramirez-Ruiz (2015); MacLeod et al. (2017); De et al. (2020) and their results are consistent with the picture where the critical cylindrical radius within which the gas gets physically captured by the neutron star is given by H_ρ instead of r_B , if $H_\rho < r_B$.

Since most of the mass is captured near the pericenter r_p of the orbit, we adopt the following estimate for the captured mass *per orbit*

$$\Delta M_{\text{cap}} \simeq \pi^2 r_p \rho(r_p) \min(H_\rho^2, r_B^2)|_{r_p}, \quad (34)$$

where we have taken a path length of πr_p near the pericenter. We emphasize that eq. (34) does not take into account the gas accumulation near the neutron star — an existing accretion disk (from earlier gas capture) may increase the effective cross-section for mass capture. We also ignore the captured mass at orbital separations much greater than r_p . For these reasons, our estimated ΔM_{cap} is likely a lower limit to the true values.

Since the neutron star moves super-sonically through the envelope, the perturbation to the envelope structure by the neutron star’s gravitational acceleration will not change our results substantially. However, we expect the modification of the envelope structure by the feedback from the accretion power to be important, for the following reason (see also Hober et al. 2022). Suppose the accretion power $L = 10^{42} L_{42} \text{ erg s}^{-1}$ is carried by an outflow with speed v_w , this produces a ram pressure at radius r from the neutron star

$$P_w = \frac{L}{4\pi r^2 v_w} \simeq 5.5 \times 10^7 \frac{\text{erg}}{\text{cm}^3} L_{42} \frac{0.1c}{v_w} \left(\frac{10R_\odot}{r} \right)^2. \quad (35)$$

This pressure P_w is comparable to the ram pressure of the Bondi-captured gas in the neutron star’s frame

$$\rho v^2 \simeq 10^8 \frac{\text{erg}}{\text{cm}^3} \rho_{-7} (v/300 \text{ km s}^{-1})^2, \quad (36)$$

where $\rho = 10^{-7} \rho_{-7} \text{ g cm}^{-3}$ is the density of the envelope near the orbital pericenter radius $r_p \simeq 10R_\odot$ (see Fig. 7) and v is the relative velocity between the gas and the neutron star.

Nevertheless, the above issues of our crude model can only be addressed by detailed numerical simulations of the interactions between a neutron star and the inflated stellar envelope, which is left for future works.

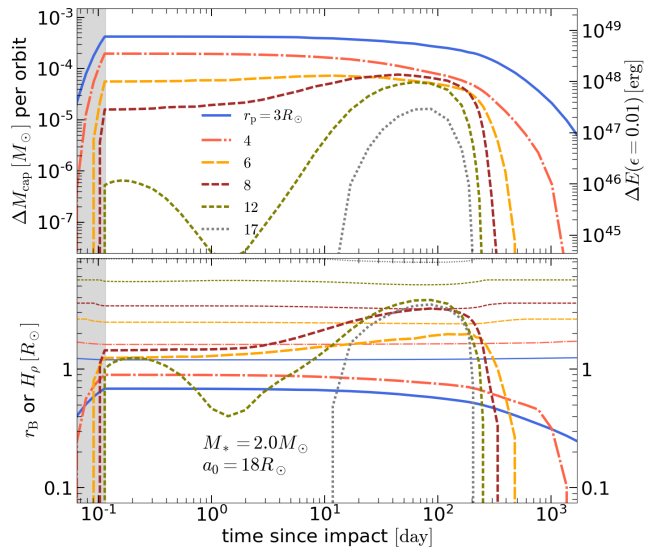


FIG. 9.— *Upper panel:* Captured mass per orbit ΔM_{cap} (eq. 34) and the energy release $\Delta E = \epsilon \Delta M_{\text{cap}} c^2$ for different pericenter radii r_p/R_\odot and a fiducial accretion efficiency $\epsilon = 0.01$. Since ΔM_{cap} only depends weakly on the post-supernova semimajor axis a (as long as the orbit is at least mildly eccentric), we fix $a = 50R_\odot$ in all cases. The companion is a $M_* = 2.0M_\odot$ main-sequence star at pre-supernova orbital separation of $a_0 = 18R_\odot$. *Lower panel:* The density scale-height H_ρ (thick lines, eq. 32) and Bondi radius r_B (thin lines, eq. 28), both evaluated at the post-supernova pericenter $r = r_p$. We find $H_\rho \lesssim r_B$ in most cases. In both panels, the gray region at $t < 10^4$ s marks the heat-injection episode.

The time evolution for the captured mass per orbit ΔM_{cap} for a $M_* = 2M_\odot$ companion star placed at a pre-supernova orbital separation of $a_0 = 18R_\odot$ (corresponding to $P_{\text{sh}} = 2.4 \times 10^{14} \text{ erg cm}^{-3}$) is shown in Fig. 9. Note that the time axis should be understood as the pericenter passage time for a hypothetical orbit — the binary orbital motion is not explicitly considered in this calculation.

For the post-supernova orbit (which depends on the unknown natal kick on the neutron star, see §6.1), we consider a wide range of pericenter radii $3 \leq r_p \leq 17R_\odot$ and fix the semimajor axis to be $a = 50R_\odot$ (the results depend weakly on a as long as $2/r_p \gg 1/a$ in eq. 27). Note that, for any natal kick, the post-supernova pericenter radius is physically constrained by $r_p \leq a_0$. On the other hand, we do not consider very small pericenter radii, because the companion star will likely be tidally disrupted by the neutron star (Perets et al. 2016; Kremer et al. 2019, 2022) and our Bondi-capture picture breaks down. The observational consequences of such tidal disruptions are calculated in detail by Tsuna & Lu (2025).

We find that, for $a_0 = 18R_\odot$, when the companion star expands to near its maximum radius, the neutron star typically captures a mass of $\Delta M_{\text{cap}} \sim 10^{-4} M_\odot$ per orbit. For an accretion efficiency $\epsilon \sim 10^{-2}$ (see §4.2 and eq. 61), then accretion onto the neutron star can produce 10^{48} erg of energy (right axis in Fig. 9).

For smaller post-supernova pericenter radii $r_p \lesssim 8R_\odot$, the mass capture starts immediately after the ejecta’s impact (i.e., in the first post-supernova orbit). This is because the radius of the shock-heated star R_* exceeds r_p by the end of the heating episode (see Fig. 2). The

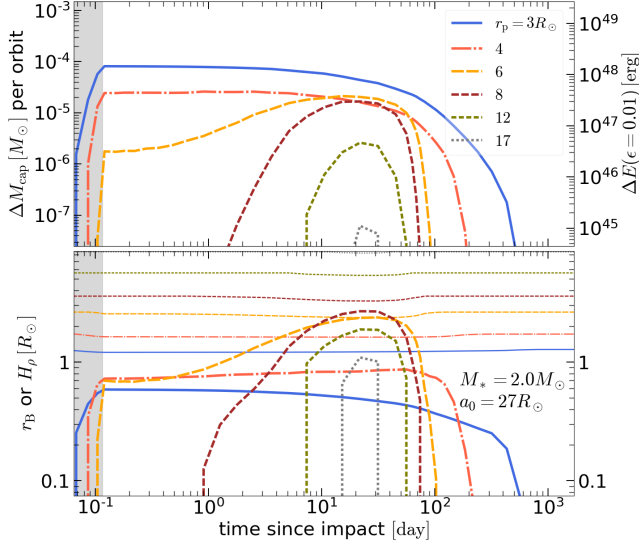


FIG. 10.— The same as Fig. 9 but for pre-supernova orbital separation of $a_0 = 27R_\odot$.

mass capture persists until $\gtrsim 1$ yr after the supernova — the time frame is longer for smaller r_p , and then the mass capture shuts off due to Kelvin-Helmholtz contraction of the shock-heated outer envelope. For larger pericenter radii $r_p \gtrsim 12R_\odot$ (green dashed lines), the strongest mass capture occurs after a substantial delay of the order 10 days to one month, and the mass capture ends abruptly after about 200 days. Later in §6, we will discuss the observational implications of such a delayed onset of neutron star accretion — such systems will produce unique, double-peaked supernova lightcurves.

In Fig. 10, we show another case for a larger pre-supernova orbital separation of $a_0 = 27R_\odot$ (corresponding to $P_{\text{sh}} = 7.4 \times 10^{13} \text{ erg cm}^{-3}$). The captured mass per orbit is significantly less than that for $a_0 = 18R_\odot$, because the envelope is less inflated under a weaker ram pressure. However, the qualitative results are similar: for smaller $r_p \lesssim 6R_\odot$, the mass capture is stronger and starts promptly; whereas for larger $r_p \gtrsim 8R_\odot$, the mass capture is weaker and reaches a peak after some delay.

In the following, we assume $H_\rho(r_p) \lesssim r_B(r_p)$ (as shown by the lower panels of Figs. 9 and 10) and calculate the specific angular momentum of the captured gas. When the neutron star reaches the pericenter, the gas located within a cylindrical radius $\tilde{r} \lesssim H_\rho(r_p)$ in the plane perpendicular to the neutron star’s velocity v will be efficiently captured. Let us denote the azimuthal angle in the perpendicular plane as $\tilde{\phi}$, with $\tilde{\phi} = 0$ corresponding to the radial direction outwards from the center of the companion star. To the linear order, the gas density in the perpendicular plane at coordinate $(\tilde{r}, \tilde{\phi})$ is given by

$$\rho(\tilde{r}, \tilde{\phi}) \approx \rho_0 - \frac{\rho_0}{H_\rho} \tilde{r} \cos \tilde{\phi}, \quad (37)$$

where $\rho_0 = \rho(r_p)$ is the stellar density at $r = r_p$ and $H_\rho = H_\rho(r_p)$. The mass capture rate is given by

$$\dot{M}_d(r_p) \simeq \int_0^{2\pi} d\tilde{\phi} \int_0^{H_\rho} d\tilde{r} \tilde{r} \rho(\tilde{r}, \tilde{\phi}) v_p, \quad (38)$$

and the angular momentum capture rate is

$$\dot{L}_d(r_p) \simeq \int_0^{2\pi} d\tilde{\phi} \int_0^{H_\rho} d\tilde{r} \tilde{r} \rho(\tilde{r}, \tilde{\phi}) v_p \tilde{r} v_p \cos \tilde{\phi}, \quad (39)$$

where $v_p = v(r_p)$ is the velocity at the pericenter and the extra factor of $\cos \tilde{\phi}$ in $\dot{L}_d(r_p)$ comes from the fact that only the angular momentum component perpendicular to the post-supernova orbital plane is non-zero. Thus, we obtain the specific angular momentum for the accretion disk around the neutron star

$$\ell_d \simeq \frac{\dot{L}_d(r_p)}{\dot{M}_d(r_p)} \simeq \frac{1}{4} H_\rho(r_p) v(r_p). \quad (40)$$

Since $v(r_p) \approx \sqrt{2G(M_{\text{ns}} + M_*)/r_p}$, we then obtain the circularization radius of the accretion disk

$$r_{d,0} = \frac{\ell_d^2}{GM_{\text{ns}}} \simeq \frac{H_\rho^2}{8r_p} \left(1 + \frac{M_*}{M_{\text{ns}}}\right). \quad (41)$$

For typical values of $H_\rho \sim 3R_\odot$, $r_p \sim 10R_\odot$, and $M_* \sim 3M_\odot$, we obtain

$$r_{d,0} \sim 0.3R_\odot. \quad (42)$$

As the disk will viscously expand over time, its size r_d is roughly given by the condition that the viscous timescale,

$$t_{\text{vis}} = \frac{1}{\alpha h^2 \Omega_K(r_d)} \simeq 0.3 \text{ d} (r_d/0.3R_\odot)^{3/2} \frac{\alpha h^2}{0.01}, \quad (43)$$

is comparable to the mass-capture timescale of $\sqrt{r_p^3/G(M_{\text{ns}} + M_*)}$, so we obtain the disk radius

$$\begin{aligned} r_d &\simeq r_p \frac{(\alpha h^2)^{2/3}}{(1 + M_*/M_{\text{ns}})^{1/3}} \\ &\simeq 0.3R_\odot \frac{r_p}{10R_\odot} \left(\frac{\alpha h^2}{0.01}\right)^{2/3} \left(\frac{3}{1 + M_*/M_{\text{ns}}}\right)^{1/3}, \end{aligned} \quad (44)$$

where α is the dimensionless viscosity parameter (Shakura & Sunyaev 1973), h is the ratio between the vertical scale height and the disk radius r_d , and $\Omega_K(r_d) = \sqrt{GM_{\text{ns}}/r_d^3}$ is the Keplerian angular frequency. Hereafter, we take $r_d \simeq 0.3R_\odot$ to be our fiducial value for the disk size.

Then, the characteristic accretion rate in the outer disk is given by

$$\dot{M}_d \simeq \frac{\Delta M_{\text{cap}}}{t_{\text{vis}}} \simeq 0.14 \frac{M_\odot}{\text{yr}} \frac{\Delta M_{\text{cap}}}{10^{-4} M_\odot} \frac{\alpha h^2/0.01}{(r_d/0.3R_\odot)^{3/2}}. \quad (45)$$

Below, we show that such a high accretion rate can potentially power very bright emission.

4.2. Accretion onto magnetized neutron star

In this section, we consider the power generated by the accretion flow around the neutron star.

The Eddington luminosity of the neutron star is given by $L_{\text{Edd}} = 4\pi GM_{\text{ns}} c / \kappa_T$, where $\kappa_T \approx 0.34 \text{ cm}^2 \text{ g}^{-1}$ is the electron scattering opacity appropriate for the accreting gas. The key property of the accretion flow is the *locally*

super-Eddington accretion rate $GM_{\text{ns}}\dot{M}(r)/r \gg L_{\text{Edd}}$ at relevant radii r between the neutron star radius R_{ns} and the disk outer radius r_{d} (eq. 44). Thermally driven outflow causes the accretion rate to drop towards smaller radii, and the self-similar solution is given by (Narayan & Yi 1995; Blandford & Begelman 1999)

$$\dot{M}(r) = \dot{M}_{\text{d}}(r/r_{\text{d}})^p, \quad (46)$$

where \dot{M}_{d} is the mass accretion rate near the disk outer radius and p is the power-law index for the radial scaling of the accretion rate. Following the results from numerical simulations (Stone et al. 1999; Stone & Pringle 2001; Yuan et al. 2012, 2015; White et al. 2020; Cho et al. 2023; Guo et al. 2024), we take $p = 0.5$ in this paper as a representative value. For completeness, we take r_{d} in the above power-law scaling to be the spherization radius $r_{\text{sph}} = GM_{\text{ns}}\dot{M}_{\text{d}}/L_{\text{Edd}}$ (Begelman 1979), when $r_{\text{sph}} < r_{\text{d}}$.

The accretion flow is truncated at the Alfvén radius r_{A} where the magnetospheric pressure overwhelms the gas pressure. For quasi-spherical accretion, this critical radius is given by (Davidson & Ostriker 1973; Ghosh & Lamb 1979; Frank et al. 2002)

$$r_{\text{A}} \simeq \left(\frac{\mu_{\text{B}}^2}{2\dot{M}(r_{\text{A}})\sqrt{2GM_{\text{ns}}}} \right)^{2/7}, \quad (47)$$

or

$$r_{\text{A}} \simeq \left(\frac{\mu_{\text{B}}^2 r_{\text{d}}^p}{2\dot{M}_{\text{d}}\sqrt{2GM_{\text{ns}}}} \right)^{\frac{2}{7+2p}}, \quad (48)$$

where $\mu_{\text{B}} = B_{\text{ns}}R_{\text{ns}}^3$ is the magnetic dipole moment of the neutron star and B_{ns} is the surface dipolar B-field strength at the magnetic equator. The corotation radius is where the Keplerian frequency is equal to the spin frequency and given by

$$r_{\text{co}} = \left(\frac{GM_{\text{ns}}}{\Omega^2} \right)^{1/3}, \quad (49)$$

where $\Omega = 2\pi/P$ is the spin angular frequency. The light cylinder radius is

$$r_{\text{lc}} = c/\Omega. \quad (50)$$

The interplay among these three radii r_{A} , r_{co} , and r_{lc} determines the total power of the neutron star accretion flow system, which consists of four components:

- (i) The electromagnetic (Poynting) power L_{m} from the open magnetic field lines, accounting for the disk-induced opening of fields (Parfrey et al. 2016; Metzger et al. 2018),

$$L_{\text{m}} = \frac{\mu_{\text{B}}^2 \Omega^4}{c^3} \max \left[1, (r_{\text{lc}}/r_{\text{A}})^2 \right]. \quad (51)$$

- (ii) The power from accretion onto the neutron star's surface

$$L_{\text{ns}} = \min \left(L_{\text{ns,max}}, \frac{GM_{\text{ns}}\dot{M}_{\text{ns}}}{R_{\text{ns}}} \right), \quad (52)$$

where $L_{\text{ns,max}} = 3.5 \times 10^{39} (B_{\text{ns}}/10^{12} \text{ G})^{3/4} \text{ erg s}^{-1}$ is the maximum luminosity from the accretion column onto the neutron star (Basko & Sunyaev 1976;

Mushtukov et al. 2015), and the surface accretion rate is given by $\dot{M}_{\text{ns}} = \dot{M}(r_{\text{A}})$ if $r_{\text{A}} < \min(r_{\text{lc}}, r_{\text{co}})$ (in the accretor state) and $\dot{M}_{\text{ns}} \approx 0$ otherwise (since very little mass will land on the neutron star). Note that when the neutron star accretes at extremely high rates, a large fraction of the accretion power is lost due to neutrino emission, which causes the radiative power to be limited to $L_{\text{ns,max}}$ (Basko & Sunyaev 1976).

- (iii) If $r_{\text{co}} < r_{\text{A}} < r_{\text{lc}}$, the system is in the propeller state, so the gas near the Alfvén radius is forced to corotate at the spin angular frequency and this forms a wind whose power is given by

$$L_{\text{w}} = (\Omega r_{\text{A}})^2 \dot{M}(r_{\text{A}}). \quad (53)$$

When the system is not in the propeller regime, we take $L_{\text{w}} = 0$.

- (iv) The disk accretion power near the Alfvén radius is given by $L_{\text{d}} = GM_{\text{ns}}\dot{M}(r_{\text{A}})/r_{\text{A}}$, where $\dot{M}(r_{\text{A}}) = \dot{M}_{\text{d}}(r_{\text{A}}/r_{\text{d}})^p$ is the accretion rate near r_{A} .

Thus, the total power from the accretion system in different states are given by

$$L \simeq \begin{cases} L_{\text{m}}, & \text{if } r_{\text{A}} > r_{\text{lc}} \text{ (pulsar)}, \\ L_{\text{m}} + L_{\text{w}} + L_{\text{d}}, & \text{if } r_{\text{co}} < r_{\text{A}} < r_{\text{lc}} \text{ (propeller)}, \\ L_{\text{m}} + L_{\text{ns}} + L_{\text{d}}, & \text{if } r_{\text{A}} < \min(r_{\text{lc}}, r_{\text{co}}) \text{ (accretor)}. \end{cases} \quad (54)$$

An important outcome is that the outflows have a wide range of velocities from $\sim \sqrt{GM_{\text{ns}}/r_{\text{d}}}$ all the way up to near the speed of light (when r_{A} is close to r_{lc} but above r_{co}). The velocity stratification leads to the formation of internal shocks when the faster components launched in a later orbit collide with the slower components launched in an earlier orbit. The emission from such internal shocks will be discussed in §5.

The neutron star's spin angular frequency Ω is affected by the spin-up and spin-down torques according to

$$I_{\text{ns}}\dot{\Omega} \simeq \begin{cases} -\frac{L_{\text{m}}}{\Omega}, & \text{if } r_{\text{A}} > r_{\text{lc}}, \\ -\frac{L_{\text{m}}}{\Omega} + \dot{M}(r_{\text{A}})r_{\text{A}}^2 [\Omega_{\text{K}}(r_{\text{A}}) - \Omega], & \text{else,} \end{cases} \quad (55)$$

where I_{ns} is the neutron star's moment of inertia, and $\Omega_{\text{K}}(r_{\text{A}}) = \sqrt{GM_{\text{ns}}/r_{\text{A}}^3}$ is the Keplerian angular frequency at the Alfvén radius. The torques follow the prescriptions by Ekşi et al. (2005); Piro & Ott (2011), although there are theoretical uncertainties about the detailed magnetosphere-disk interactions near the Alfvén radius (e.g., Wang 1995; Lovelace et al. 1995; Miller & Stone 1997; Romanova et al. 2004; Parfrey & Tchekhovskoy 2017).

When the electromagnetic torque $-L_{\text{m}}/\Omega$ is negligible compared to other components, the equilibrium spin frequency $\tilde{\Omega}_{\text{eq}}$ is given by $r_{\text{A}} = r_{\text{co}}(\tilde{\Omega}_{\text{eq}})$, or

$$\tilde{\Omega}_{\text{eq}} = \frac{2\pi}{\tilde{P}_{\text{eq}}} = (GM_{\text{ns}})^{\frac{5+p}{7+2p}} \left(\frac{\dot{M}_{\text{d}}}{\mu_{\text{B}}^2 r_{\text{d}}^p} \right)^{\frac{3}{7+2p}}. \quad (56)$$

In reality, the true equilibrium spin frequency Ω_{eq} as

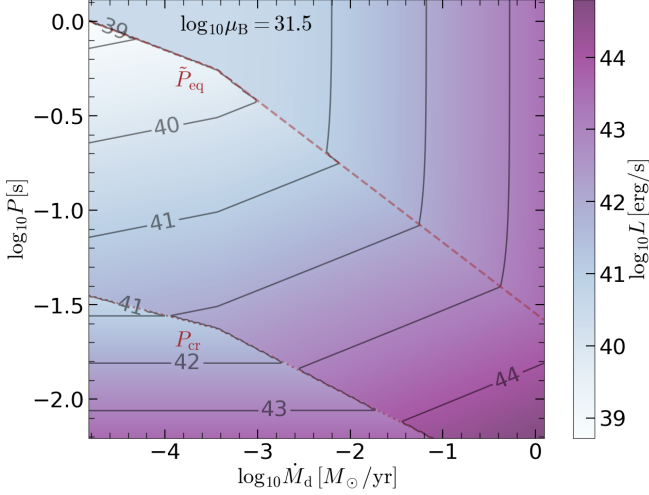


FIG. 11.— Total power from the neutron star-disk system as a function of the accretion rate in the outer disk \dot{M}_d and the spin period $P = 2\pi/\Omega$. We fix the following parameters: magnetic dipole moment $\mu_B = 10^{31.5} \text{ G cm}^3$ (similar to the Crab Pulsar), index for the radial scaling of the accretion rate $p = 0.5$, and the outer disk radius $r_d = R_\odot$. The system may be in three different states: pulsar state ($P < P_{\text{cr}}$ region), propeller state ($P_{\text{cr}} < P < \tilde{P}_{\text{eq}}$ region), and accretor state ($P > \tilde{P}_{\text{eq}}$ region).

given by $\dot{\Omega} = 0$ is slightly different from $\tilde{\Omega}_{\text{eq}}$. Nevertheless, $\tilde{\Omega}_{\text{eq}}$ is important as it separates the propeller state from the accretor state. Another critical spin frequency Ω_{cr} is given by $r_A = r_{\text{lc}}$, which sets the boundary between the pulsar state ($r_A > r_{\text{lc}}$) and the propeller/accretor states ($r_A < r_{\text{lc}}$), and we have

$$\Omega_{\text{cr}} = 2\pi/P_{\text{cr}} = c/r_A. \quad (57)$$

The total power of the system as a function of the accretion rate of the outer disk \dot{M}_d and the neutron star's spin period is shown in Fig. 11. We find that, for a modest magnetic dipole moment $\mu_B = 10^{31.5} \text{ G cm}^3$ (or $B_{\text{ns}} \simeq 3 \times 10^{13} \text{ G}$), spin period $P \sim 30 \text{ ms}$ (similar to the Crab Pulsar), and accretion rates $\dot{M}_d \gtrsim 10^{-2} M_\odot \text{ yr}^{-1}$, it is possible to obtain very high powers $L \gtrsim 10^{42.5} \text{ erg s}^{-1}$ in the propeller state. Such accretion rates are achievable based on the interactions between the neutron star and the inflated envelope of the companion star (see eq. 45). In the propeller state, most of the power comes from the rotational energy of the neutron star (meaning that L_w dominates over L_m and L_d), and the accretion flow taps the rotational energy faster than the magnetic dipole emission.

The timescale for the neutron star's spin evolution $\Omega/|\dot{\Omega}|$ is shown in Fig. 12. For $\mu_B = 10^{31.5} \text{ G cm}^3$, the spin evolution timescale is generally longer than 10^2 d for accretion rates $\dot{M}_d \lesssim 0.1 M_\odot \text{ yr}^{-1}$, so spin evolution occurs on timescales comparable or longer than the evolutionary timescale of the accretion rate.

We define the accretion efficiency of the system as

$$\epsilon \equiv \frac{L_{\text{acc}}}{\dot{M}_d c^2} \equiv \frac{L_w + L_{\text{ns}} + L_d}{\dot{M}_d c^2}, \quad (58)$$

which does not include the electromagnetic power L_m (which is negligible in our calculations). From Fig. 11,

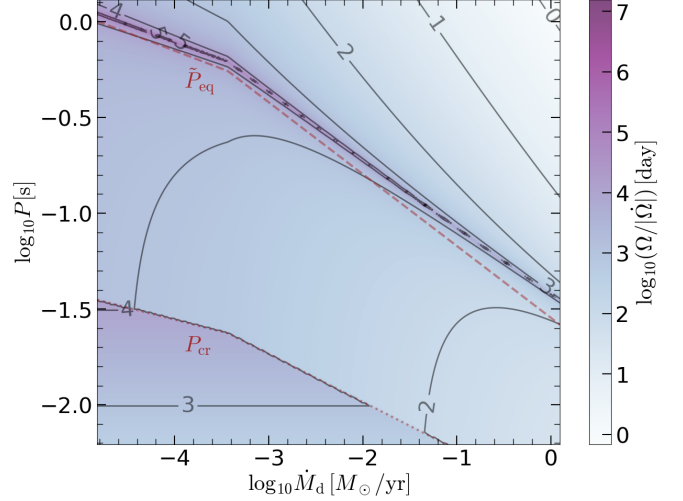


FIG. 12.— The timescale for spin evolution $\Omega/|\dot{\Omega}|$ for the same system shown in Fig. 11. Note that, due to a non-zero electromagnetic spin-down torque $-L_m/\Omega$ (eq. 55), the spin equilibrium at $\dot{\Omega} = 0$ does not coincide with the dashed line for $P = \tilde{P}_{\text{eq}}$.

we see that the accretion luminosity L_{acc} is maximized when $P = P_{\text{cr}}$ or the light cylinder coincide with the Alfvén radius $r_{\text{lc}} = r_A$. When this occurs, the gas that reaches down to the Alfvén radius is flung away at the corotational speed which is close to the speed of light. To correctly obtain the system's total power, a fully relativistic calculation is required — our Newtonian treatment is only applicable when the spin period is slightly longer than the critical period P_{cr} . At $P = P_{\text{cr}}$, the ratio between the electromagnetic power and the propeller wind power is given by⁴

$$\begin{aligned} \frac{L_m}{L_w}(P = P_{\text{cr}}) &= 2\sqrt{2GM_{\text{ns}}/(r_{\text{lc}}c^2)} \\ &= 2\sqrt{2r_g/r_{\text{lc}}} = 0.11(P/30\text{ms})^{-1/2}, \end{aligned} \quad (59)$$

where $r_g = GM_{\text{ns}}/c^2$ is the gravitational radius of the neutron star. The ratio between the disk accretion power and the propeller wind power is given by

$$\frac{L_d}{L_w}(P = P_{\text{cr}}) = r_g/r_{\text{lc}} = 1.4 \times 10^{-3}(P/30\text{ms})^{-1}. \quad (60)$$

Therefore, for sufficiently slow pulsars $P \gtrsim 10 \text{ ms}$, we find that the total power is dominated by the propeller wind $L \approx L_w \approx M(r_{\text{lc}})c^2$ when $P = P_{\text{cr}}$. Thus, the maximum accretion efficiency is given by

$$\epsilon_{\text{max}} \approx \left(\frac{r_A}{r_d}\right)^p = 3.9\% \dot{M}_{d,-1}^{-\frac{1}{8}} \mu_{B,31.5}^{\frac{1}{4}} \left(\frac{r_d}{0.3R_\odot}\right)^{-\frac{7}{16}}, \quad (61)$$

where we have used $\dot{M}_d = 10^{-1} M_\odot \text{ yr}^{-1} \dot{M}_{d,-1}$, $\mu_B = 10^{31.5} \text{ G cm}^3 \mu_{B,31.5}$, and $p = 0.5$. For a more optimistic case of $p = 0.3$, we obtain $\epsilon_{\text{max}} \approx 12.7\% \dot{M}_{d,-1}^{-0.08} \mu_{B,31.5}^{0.16} (r_d/0.3R_\odot)^{-0.28}$.

⁴ At $P < P_{\text{cr}}$, the disk truncates at $r_A > r_{\text{lc}}$ and the accreting gas is not forced into corotation with the magnetosphere, so the propeller wind disappears. This might be an artifact of our current model for the propeller state. Future theoretical works should address if this discontinuity is real.

The above estimate shows that ϵ_{\max} is relatively insensitive to the highly uncertain accretion rate \dot{M}_d and magnetic dipole moment μ_B . Since our Bondi-capture picture gives a robust disk radius of $r_d \sim 0.3R_\odot$ (see eq. 44), we conclude that the accretion system has a maximum efficiency of a few percent (for $p = 0.5$), which is achieved when the system is in the propeller state near the boundary of the pulsar state $P \simeq P_{\text{cr}}$. Away from the boundary of $P = P_{\text{cr}}$ but still in the propeller state, the efficiency is given by

$$\epsilon/\epsilon_{\max} = (r_A/r_{\text{lc}})^2 = (P/P_{\text{cr}})^{-2}. \quad (62)$$

We see that the accretion efficiency drops as $\epsilon \propto P^{-2}$ for longer spin periods if we keep \dot{M}_d , r_d , and μ_B fixed. On the other hand, if we keep P , r_d , and μ_B fixed, the accretion efficiency scales as $\epsilon \propto \dot{M}_d^{-1/2}$ (for $p = 0.5$).

On the other hand, in the limit of an extremely slow spin or weak magnetic dipole moment, we obtain the minimum accretion efficiency for $p = 0.5$,

$$\epsilon_{\min} = \left(\frac{R_{\text{ns}}}{r_d}\right)^p \frac{r_g}{R_{\text{ns}}} \simeq 1.3 \times 10^{-3} (r_d/0.3R_\odot)^{-1/2}. \quad (63)$$

We note that the minimum efficiency is likely too small to power the second peak in SN2022jli, unless the accretion power-law index is smaller $p < 0.5$ or the captured mass per orbit is as large as $\Delta M_{\text{cap}} \sim 10^{-3}M_\odot$.

In the next section, we discuss how the accretion power may be converted into observable radiation, while keeping our discussion agnostic to the detailed disk outflow launching mechanisms (propeller- or viscously-driven wind).

5. EMISSION FROM SHOCKS

The accretion-driven outflow launched near disk radius r has mass loss rate $\dot{M}(r) = \dot{M}_d(r/r_d)^p$ and speed $v(r)$. At large radii $r \gg r_d$, the outflow will be radially stratified due to the velocity difference. The fastest outflow that carries the majority of the accretion power will collide with slower material on its way outward. There are two locations for energy dissipation: (1) for a bound post-supernova orbit, disk accretion occurs periodically on the orbital timescale, so the slower outflow from an earlier episode will lie ahead of the freshly launched faster outflow; (2) the cumulative disk outflow will collide with the supernova ejecta at much larger radii. The geometry of the system is schematically shown in Fig. 13. These collisions create shocks that dissipate the outflow's kinetic energy into heat. If the cooling timescale of the shock-heated gas is shorter than the dynamical expansion timescale, such shocks have a high radiative efficiency, so bright emission will be produced. In the following, we first focus on the internal shocks that form due to the collisions between adjacent episodes of disk outflows and then briefly comment on the radiative efficiency of the wind-ejecta shocks. We consider the cooling of the thermal and non-thermal electrons in §5.1 and 5.2, respectively.

5.1. Cooling of thermal electrons

The fastest outflow, originated from near the Alfvén radius, can reach up to a significant fraction of c in the

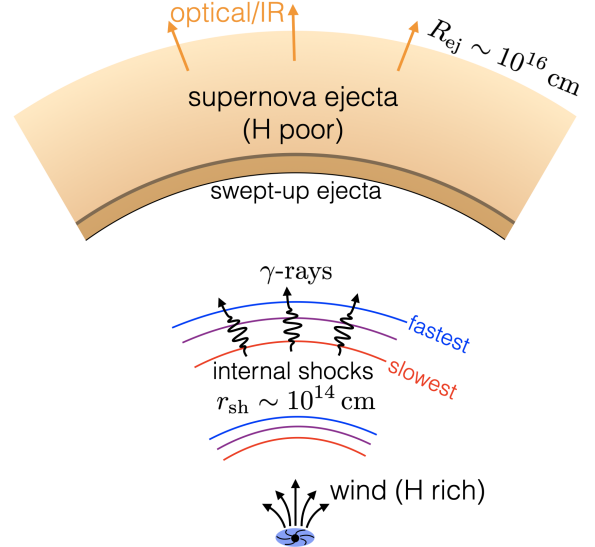


FIG. 13.— Geometry of the system on lengthscales from 10^{14} to 10^{16} cm.

extreme limit (if $r_A \simeq r_{\text{lc}}$). The slowest outflow is launched from the outer disk near $r \sim r_d \sim 0.3R_\odot$, so the minimum speed is of the order $v_{\min} \sim \sqrt{GM_{\text{ns}}/r_d} \sim 10^8 \text{ cm s}^{-1}$ (roughly the local Keplerian speed). For a post-supernova orbital period of $P = 10P_{10\text{d}}$ day, the internal shocks occur at a characteristic radius

$$r_{\text{sh}} \simeq v_{\min} P \sim 10^{14} \text{ cm } P_{10\text{d}}. \quad (64)$$

The total gas mass ejected in each binary orbit is of the order ΔM_{cap} , and the total energy carried by the fastest outflow is of the order

$$\Delta E \sim \epsilon \Delta M_{\text{cap}} c^2 = 1.8 \times 10^{48} \text{ erg } \epsilon_{-2} \frac{\Delta M_{\text{cap}}}{10^{-4} M_\odot}, \quad (65)$$

where ϵ is the accretion efficiency, and we have taken $\epsilon = 10^{-2} \epsilon_{-2}$ (eq. 58). We assume that an order-unity fraction of the ejected mass is swept up by the forward shock and expands at speed

$$v_{\text{exp}} \simeq 0.1 c \epsilon_{-2}^{1/2}. \quad (66)$$

Thus, the dynamical expansion timescale of the shock-heated gas is given by

$$\begin{aligned} t_{\text{dy}} &= \max[t_{\text{vis}}, r_{\text{sh}}/v_{\text{exp}}] \\ &= \max\left[0.3 \text{ d } \frac{(r_d/0.3R_\odot)^{3/2}}{\alpha h^2/0.01}, 0.4 \text{ d } r_{\text{sh},14} \epsilon_{-2}^{-1/2}\right], \end{aligned} \quad (67)$$

where we have assumed that most of the accretion energy is injected on the viscous timescale t_{vis} (eq. 43).

Let us denote the shock speed as βc , which is measured in the frame of the unshocked gas. Below, we take $\beta = 0.1\beta_{0.1}$ to be a typical fiducial value for the forward shock that propagates into the slower, denser outflow component. We note that the reverse shock crossing the faster outflow may have a higher β , and the cooling of reverse shock-heated gas (dominated by inverse-Compton scattering) requires a strong radiation field that is provided by free-free emission by the much denser forward

shock-heated gas. The following discussion on inverse-Compton cooling applies to electrons heated by both forward and reverse shocks.

For a given shock speed βc , the shock-heated gas has temperature

$$T_{\text{sh}} = \frac{3\mu m_{\text{p}}(\beta c)^2}{16k_{\text{B}}} = 1.2 \times 10^{10} \text{ K } \beta_{0.1}^2. \quad (68)$$

We assume that electrons and ions reach an equilibrium⁵ with the same kinetic temperature T_{sh} . The Thomson scattering optical depth for the slowest disk outflow heated by the forward shock is given by

$$\tau_{\text{s}} \simeq \frac{\kappa_{\text{T}} \Delta M_{\text{cap}}}{4\pi r_{\text{sh}}^2} \simeq 0.5 \frac{\Delta M_{\text{cap}}}{10^{-4} M_{\odot}} r_{\text{sh},14}^{-2}, \quad (69)$$

where we have taken the Thomson opacity $\kappa_{\text{T}} \simeq 0.34 \text{ cm}^2 \text{ g}^{-1}$ for solar metallicity. Klein-Nishina effects further suppress the scattering cross-section, making the shock-heated region even more optically thin.

The relevant processes for electron cooling are free-free emission and inverse-Compton scattering. For sufficiently high shock speeds $\beta \gtrsim 0.1$ and low scattering optical depths $\tau_{\text{s}} \lesssim 1$, inverse-Compton cooling generally dominates over free-free cooling (see [Margalit et al. 2022](#), who treat the Comptonization of free-free photons in detail).

The hydrogen number density in the forward shock-heated region is roughly given by

$$n \sim \frac{\Delta M_{\text{cap}}}{V_{\text{sh}} m_{\text{p}}} \sim 1 \times 10^{11} \text{ cm}^{-3} r_{\text{sh},14}^{-3} \frac{\Delta M_{\text{cap}}}{10^{-4} M_{\odot}}, \quad (70)$$

where we have taken the volume of the shock-compressed gas to be $V_{\text{sh}} \sim r_{\text{sh}}^3$. The total free-free luminosity is then given by

$$\begin{aligned} L_{\text{ff}} &= 4\pi j_{\text{ff}} V_{\text{sh}} f_{\text{rel,ff}} \\ &\simeq 3 \times 10^{42} \text{ erg s}^{-1} \beta_{0.1} r_{\text{sh},14}^{-3} \frac{f_{\text{rel}}}{2} \left(\frac{\Delta M_{\text{cap}}}{10^{-4} M_{\odot}} \right)^2, \end{aligned} \quad (71)$$

where f_{rel} is a correction factor that smoothly connects the non-relativistic to the relativistic regimes

$$f_{\text{rel,ff}} \simeq 1 + \frac{1.3(T_{\text{sh}}/10^{10} \text{ K})}{1 + 0.6(T_{\text{sh}}/10^{10} \text{ K})^{1/2}}. \quad (72)$$

Then, the photon energy density photons from free-free emission is given by (in the optically thin limit)

$$\begin{aligned} U_{\text{ff}} &\simeq L_{\text{ff}} / (4\pi r_{\text{sh}}^2 c) \\ &\simeq 800 \text{ erg cm}^{-3} \beta_{0.1} r_{\text{sh},14}^{-5} \frac{f_{\text{rel}}}{2} \left(\frac{\Delta M_{\text{cap}}}{10^{-4} M_{\odot}} \right)^2. \end{aligned} \quad (73)$$

Although free-free emission alone is unable to efficiently cool the shock-heated electrons, inverse-Compton scattering of these seed photons is more efficient and the

⁵ If electron temperature T_e is less than the ion temperature T_i (numerical simulations suggest $0.2 \lesssim T_e/T_i \lesssim 1$, e.g., [Spitkovsky 2008](#); [Kato & Takabe 2010](#); [Park et al. 2015](#); [Crumley et al. 2019](#)), we should roughly replace T_{sh} by T_e . The thermal electrons still cool efficiently, but the overall radiative efficiency of internal shocks will be smaller by a factor of a few.

corresponding cooling time is

$$\begin{aligned} t_{\text{IC}} &= \frac{3m_e c^2}{8U_{\text{ff}} \sigma_{\text{T}} c} f_{\text{rel,IC}}^{-1} \\ &\simeq 0.02 \text{ d} \left(\frac{f_{\text{rel,IC}}}{10} \right)^{-1} \left(\frac{U_{\text{ff}}}{10^3 \text{ erg cm}^{-3}} \right)^{-1}, \end{aligned} \quad (74)$$

where $f_{\text{rel,IC}}$ is a relativistic correction factor,

$$f_{\text{rel,IC}} \simeq 1 + \frac{4k_{\text{B}} T_{\text{sh}}}{m_e c^2} = 1 + 8.1 \beta_{0.1}^2. \quad (75)$$

The above estimate does not take into account the effects of electron recoil or Klein-Nishina suppression of the scattering cross-section. We expect the scattering of the photons near the maximum frequency of the free-free spectrum $h\nu_{\text{max}} \sim k_{\text{B}} T_{\text{sh}} \sim 1 \text{ MeV}$ to be Klein-Nishina suppressed, which will reduce the inverse-Compton power by a factor of a few to 10. However, since the Compton- y parameter of the forward shock-heated region is much greater than unity,

$$y \simeq 16 \left(\frac{k_{\text{B}} T_{\text{sh}}}{m_e c^2} \right)^2 \tau_{\text{s}} \simeq 35 \beta_{0.1}^4 r_{\text{sh},14}^{-2} \frac{\Delta M_{\text{cap}}}{10^{-4} M_{\odot}}, \quad (76)$$

the lower energy free-free photons will be significantly upscattered. As long as the energy density of soft photons at $h\nu \ll m_e c^2$ exceeds $\sim 50 \text{ erg cm}^{-3}$, inverse-Compton scattering will efficiently cool the thermal electrons heated by both reverse shock and forward shock on a timescale t_{IC} that is shorter than the dynamical expansion time t_{dy} (eq. 67).

Synchrotron emission may also provide significant significant source photons for inverse-Compton cooling. Although the synchrotron photons by thermal electrons are mainly in the radio band and thus are self-absorbed, higher-frequency synchrotron emission by non-thermal electrons will be inverse-Compton scattered by thermal electrons. However, we do not discuss the synchrotron self-Compton cooling in detail here.

Based on the above discussion, we conclude that the internal shocks between adjacent episodes of mass ejections from the accretion disk are radiatively efficient — an order unity fraction of the kinetic energy of the fastest outflow will be converted into radiation. Most of the emitted energy is carried by photons near $h\nu \sim k_{\text{B}} T_{\text{sh}} \sim 1 \text{ MeV}$ (limited by electron recoiling). As long as the MeV photons efficiently deposit their energy into the supernova ejecta via Compton heating (which is the case in the first 100–300 days for typical Type Ib/c supernovae, e.g., [Wheeler et al. 2015](#)), we expect bright optical emission to be produced.

The discussion above focused on the emission from internal shocks. In the following, we briefly discuss another location for energy dissipation — the shock driven into the supernova ejecta, whose mass is mostly located at much larger radii $\gg r_{\text{sh}}$.

Let us denote the remaining energy of the accretion-driven outflow as E_{w} , which is comparable to the cumulative energy output from accretion, as the radiative losses of internal shocks can only deplete the thermal

energy of the shock-heated gas but not the kinetic energy of the bulk motion. We assume a uniform unperturbed ejecta density profile, with the location of the shock-heated ejecta at

$$r_{\text{sh,ej}}(t) \simeq \left(\frac{E_{\text{w}}}{E_{\text{ej}}}\right)^{1/5} R_{\text{ej}}(t) \\ \simeq 3 \times 10^{15} \text{ cm} \frac{t}{100 \text{ d}} \frac{v_{\text{ej}}}{10^9 \text{ cm s}^{-1}} \left(\frac{E_{\text{w},49}}{E_{\text{ej},51}}\right)^{1/5}, \quad (77)$$

where $R_{\text{ej}} = v_{\text{ej}}t$ is the characteristic radius of the ejecta, $v_{\text{ej}} \simeq \sqrt{2E_{\text{ej}}/M_{\text{ej}}}$, and t is the time since explosion. Using the same method as above, we estimate the free-free cooling timescale of the shock-heated ejecta to be

$$t_{\text{ff,ej}} \simeq 10 \text{ d} (t/100 \text{ d})^3 \frac{8}{\bar{Z}} \frac{E_{\text{ej},51}^{3/2}}{(M_{\text{ej}}/3M_{\odot})^{5/2}}, \quad (78)$$

where $\bar{Z} \simeq 8$ is the mean charge number of the ions for an oxygen-dominated composition that is fully ionized. We see that the shock propagating into the supernova ejecta is a radiative one due to rapid cooling ($t_{\text{ff,ej}} \ll t$). The typical shock velocity is given by $(r_{\text{sh,ej}}/R_{\text{ej}})v_{\text{ej}} \sim 0.01c$, so the free-free emission will be in the X-ray band at $h\nu \lesssim 10 \text{ keV}$ — these photons will deposit a fraction of their energies into the supernova ejecta by bound-free absorption (mainly by Fe group elements).

We conclude that both the internal shocks within the episodic accretion outflows (occurring at radii $r_{\text{sh}} \sim 10^{14} \text{ cm}$) and the shock propagate into the supernova ejecta (at radii $r_{\text{sh,ej}} \sim \text{few} \times 10^{15} \text{ cm}$) can efficiently dissipate and then radiate away the kinetic energy of the accretion outflow. The radiation will then be reprocessed into the optical band by the supernova ejecta. Note that only the emission from internal shocks will be modulated by the orbital period of the post-supernova binary. In the optical band, the amplitude of periodic modulation is diluted as the light-crossing time of the ejecta,

$$t_{\text{lc}} = R_{\text{ej}}/c \simeq 3 \text{ d} (t/100 \text{ d})(v_{\text{ej}}/10^9 \text{ cm s}^{-1}), \quad (79)$$

and is much longer than the timescale over which the emission from internal shocks are produced ($t_{\text{dy}} \lesssim 1 \text{ day}$, eq. 67). At sufficiently late times such that $t_{\text{lc}} \gtrsim P$, the reprocessed emission will be severely smeared and the periodic modulation in the optical band disappears.

5.2. High-energy emission by non-thermal particles

The internal shocks between adjacent episodes of disk outflows are collisionless because the gas has low scattering optical depth (eq. 69). We expect such collisionless shocks to accelerate non-thermal electrons and protons, which take fractions ϵ_e and ϵ_p of the thermal energy in the shock-heated region, respectively. Previous theoretical and observational work on shock-accelerated cosmic rays suggest $\epsilon_p \sim 0.1$, but ϵ_e remains uncertain and might be much lower (likely due to inefficient injection for diffusive shock acceleration, e.g., Park et al. 2015).

In the following, we consider the radiation from the non-thermal particles accelerated by internal shocks.

Without considering radiative losses, the maximum energy for a cosmic ray particle of charge Ze is given by the Hillas (1984) criterion (the Larmor radius $\sim r_{\text{sh}}$),

$$\mathcal{E}_{\text{max}} \sim eBr_{\text{sh}} \sim 1 \text{ EeV} Z \left(\frac{\epsilon_{\text{B},-4}\epsilon_{-2}}{r_{\text{sh},14}} \frac{\Delta M_{\text{cap}}}{10^{-4}M_{\odot}}\right)^{1/2}, \quad (80)$$

where we have taken the energy density of the magnetic field $B^2/8\pi$ in the shocked gas to be a fraction $\epsilon_{\text{B}} = 10^{-4}\epsilon_{\text{B},-4}$ of the total energy density $U \sim \epsilon\Delta M_{\text{cap}}c^2/V_{\text{sh}}$. Another criterion for the maximum energy of electrons is set by synchrotron losses. Setting the gyration of the angular frequency to be equal to the inverse of the synchrotron cooling time, we obtain the following

$$\mathcal{E}_{e,\text{max}} \sim \sqrt{\frac{e}{6\pi B\sigma_{\text{T}}}} m_e c^2 \\ \sim 0.4 \text{ TeV} \left(\frac{\epsilon_{\text{B},-4}\epsilon_{-2}}{r_{\text{sh},14}^3} \frac{\Delta M_{\text{cap}}}{10^{-4}M_{\odot}}\right)^{1/2}. \quad (81)$$

We see that cosmic ray protons can reach up to $\sim \text{EeV}$ whereas the energies of cosmic ray electrons are limited to be sub-TeV.

The cooling of ultra-relativistic electrons is dominated by synchrotron emission, as Compton scattering is suppressed by Klein-Nishina effects. This means that the emission from cosmic ray electrons will be a power-law extending up to the synchrotron burn-off limit at $9m_e c^2/(4\alpha_{\text{f}}) = 160 \text{ MeV}$ (de Jager et al. 1996), where α_{f} is the fine-structure constant.

The cooling of cosmic ray protons is dominated by inelastic collisions with other non-relativistic protons (hereafter pp collisions). The cross-section for pp collisions above an incident kinetic energy of a few GeV is about $\sigma_{pp} \gtrsim 3 \times 10^{-26} \text{ cm}^{-2}$ (Kamae et al. 2006), with a logarithmic increase at higher energies. The mean-free time between adjacent pp collisions is given by

$$t_{pp} = \frac{1}{n\sigma_{pp}c} \lesssim 0.1 \text{ d} n_{11}^{-1}. \quad (82)$$

The fact that t_{pp} is much shorter than the dynamical expansion time t_{dy} (eq. 67) means that protons with $\mathcal{E}_{\text{kin}} \gtrsim \text{GeV}$ will efficiently convert their kinetic energies into pions, π^0 and π^{\pm} . In about 1/3 of the cases, neutral pions π^0 will be produced and they subsequently decay into photons in a broad energy band from 100 MeV up to about 10 PeV, with the upper limit due to maximum proton energy limited by the short timescale for pp collisions ($\mathcal{E}_{p,\text{max}} \sim 100 \text{ PeV}$ for our fiducial parameters). Most of the radiation energy will be in the GeV band. In about 2/3 of the cases, charged pions π^{\pm} will be produced and they subsequently decay into e^{\pm} and neutrinos (with roughly equal energy between the two decay products). The e^{\pm} will then cool by synchrotron emission and produce low-energy photons. Including the photon emission from π^0 decays and cooling of secondary e^{\pm} , we find that the radiative efficiency of cosmic ray protons to be rather high, $\epsilon_{p \rightarrow \gamma} \sim 2/3$.

For cosmic ray proton energy partition $\epsilon_p = 0.1\epsilon_{p,-1}$ and

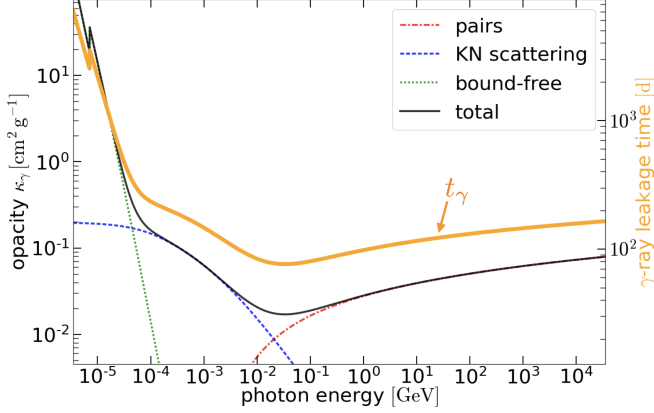


FIG. 14.— Opacity at high photon energies for a mock supernova ejecta composition: 10% He, 30% C, 40% O, 10% Ne, 5% Si, and 5% Fe-group. The sources of opacity include Bethe-Heitler pair production (Hubbell et al. 1980) in red dash-dotted line, Klein-Nishina (KN) electron scattering (Rybicki & Lightman 1986) in blue dashed line, and bound-free (bf) absorption (Verner et al. 1996) in green dotted line, and the black solid line shows the sum of all. The thick orange line shows the γ -ray leakage time t_γ in days (eq. 84) on the right axis, for ejecta mass $M_{\text{ej}} = 3M_\odot$ and energy $E_{\text{ej}} = 10^{51}$ erg. Here, we assume a spatially uniform composition, whereas realistic ejecta has more centrally concentrated Si and Fe distributions, so t_γ should be slightly longer than our estimate.

the efficiency of GeV gamma-ray emission $\epsilon_{\text{GeV}} \sim 1/3$, we estimate the orbit-averaged luminosity in the GeV band to be

$$\begin{aligned} L_{\text{GeV}} &= \frac{\epsilon_{\text{GeV}} \epsilon_p \epsilon \Delta M_{\text{cap}} c^2}{P} \\ &= 7 \times 10^{40} \text{ erg s}^{-1} \frac{\epsilon_{\text{GeV}}}{1/3} \epsilon_{p,-1} \epsilon^{-2} \frac{\Delta M_{\text{cap}}}{10^{-4} M_\odot} \frac{10 \text{ d}}{P}. \end{aligned} \quad (83)$$

The secondary neutrinos, which take away a fraction $\epsilon_{p \rightarrow \nu} \sim 1/3$ of the cosmic ray protons' energy, will also have a broad energy spectrum between 100 MeV and 10 PeV. These neutrinos, with a luminosity that is comparable to L_{GeV} above, are a smoking-gun signature of pp collisions in our model. Future observations of the PeV neutrino emission (by Icecube, Aartsen et al. 2017) will provide a decisive test of our model.

The escaping of the high-energy photons depends on the opacity of the supernova ejecta. In Fig. 14, we show the opacity as a function of photon energy for a mock supernova ejecta composition motivated by the simulations by Dessart et al. (2015b, their 5p11 model). The sources of opacities include bound-free transitions, Klein-Nishina scattering, and pair production due to collisions with nuclei and electrons. For the bound-free opacity, we assume all species are in their atomic form, but the result at $\mathcal{E}_\gamma \gtrsim \text{keV}$ is not sensitive to the ionization state of outer-shell electrons. Additionally, the opacity at $\mathcal{E}_\gamma \gtrsim 0.1 \text{ MeV}$ is not sensitive to the detailed mass composition.

For a homologously expanding ejecta with a uniform density profile, the time at which the optical depth for centrally produced γ -rays reaches $\tau_\gamma = 1$ is given by

$$t_\gamma = \left(\frac{9}{40\pi} \frac{\kappa_\gamma M_{\text{ej}}^2}{E_{\text{ej}}} \right)^{1/2} \simeq 100 \text{ d} \kappa_{\gamma,0.03}^{1/2} E_{\text{ej},51}^{-1/2} \frac{M_{\text{ej}}}{3M_\odot}, \quad (84)$$

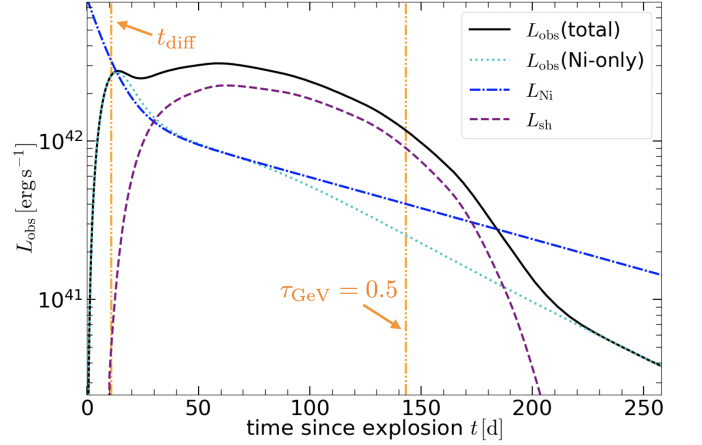


FIG. 15.— Crude model lightcurve with parameters $\epsilon = 3\%$ (accretion efficiency), $P_{\text{orb}} = 10 \text{ d}$, $M_* = 2M_\odot$, $a_0 = 18R_\odot$, $r_p = 12R_\odot$, $M_{\text{ej}} = 3M_\odot$, $M_{\text{Ni}} = 0.1M_\odot$, $E_{\text{ej}} = 10^{51}$ erg (motivated by Woosley et al. 2021). We mark the time when the optical depth for GeV photons drops to $\tau_{\text{GeV}} = 0.5$.

where $\kappa_\gamma = 0.03 \text{ cm}^2 \text{ g}^{-1} \kappa_{\gamma,0.03}$ is the opacity near photon energy of 1 GeV (Fig. 14). For a more highly centrally concentrated density profile and compositional distribution of heavier elements like Si and Fe, the γ -ray leakage time may be larger by a factor of ~ 2 . Nevertheless, we expect the GeV photons to leak out of the ejecta after a delay of the order 100 days, which is comparable to the timescale t_{max} (eq. 25) for the impacted companion star to expand to its maximum radius. This means that it is possible to detect GeV emission from the system by e.g., Fermi LAT (Atwood et al. 2009).

At even higher energies $\mathcal{E}_\gamma \sim \text{TeV}$, it takes longer for the γ -rays to leak out ($\kappa_\gamma \simeq 0.06 \text{ cm}^2 \text{ g}^{-1}$ at 1 TeV). However, pair production by $\gamma + \gamma \rightarrow e^\pm$ (not included in Fig. 14) becomes important due to the abundant optical photons, so we do not expect to detect TeV photons from the system. We also do not expect to detect X-ray photons with energies $\lesssim 30 \text{ keV}$, as they are fully trapped by the ejecta for many years, which is longer than the duration of the accretion from the companion star.

5.3. Lightcurve model

In this subsection, we attempt to construct a very crude model for the optical lightcurve of the system, leaving to future works the detailed consideration of the periodic ejecta heating due to episodic internal shocks. Our results, as shown in Fig. 15, are obtained as follows.

The UV-optical-infrared “bolometric” luminosity from the system is given by (Arnett 1982, their eq. 36 but with a general heating rate)

$$L_{\text{obs}}(t) = 2e^{-x^2} \int_0^x L_h(x' t_{\text{diff}}) e^{x'^2} x' dx', \quad (85)$$

where t is the observer's time since the explosion, $L_h(t' = x' t_{\text{diff}})$ is a centrally located heating rate at time $t' \in (0, t)$, and $x \equiv t/t_{\text{diff}}$ is the dimensionless time variable

scaled to the diffusion time⁶ for optical photons

$$t_{\text{diff}} \simeq 0.3 \left(\frac{\kappa_{\text{opt}} M_{\text{ej}}^{3/2}}{E_{\text{ej}}^{1/2} c} \right)^{1/2} \quad (86)$$

$$\simeq 11 \text{ d} \left(\frac{\kappa_{\text{opt}}}{0.02 \text{ cm}^2/\text{g}} \right)^{1/2} \left(\frac{M_{\text{ej}}}{3M_{\odot}} \right)^{3/4} E_{\text{ej},51}^{-1/4},$$

where the fiducial value for the opacity for optical photons κ_{opt} is motivated by Wheeler et al. (2015); Dessart et al. (2015b).

The heating rate includes two components

$$L_{\text{h}} = (1 - e^{-\tau_{\text{MeV}}}) L_{\text{Ni}} + L_{\text{sh}}. \quad (87)$$

The first term comes from the ^{56}Ni decay chain (Nadyozhin 1994)

$$\frac{L_{\text{Ni}}(t')}{10^{42} \text{ erg/s}} \approx \left(6.45e^{-t'/t_{\text{Ni}}} + 1.45e^{-t'/t_{\text{Co}}} \right) \frac{M_{\text{Ni}}}{0.1M_{\odot}}, \quad (88)$$

where M_{Ni} is the total mass of ^{56}Ni and the decay timescales are $t_{\text{Ni}} = 8.8 \text{ d}$ and $t_{\text{Co}} = 111.3 \text{ d}$. The optical depth τ_{MeV} accounts for the leakage effect for $\sim \text{MeV}$ γ -rays produced in the decays, with

$$\tau_{\text{MeV}} \approx (t'/t_{\text{MeV}})^{-2}, \quad (89)$$

where the leakage time t_{MeV} is obtained from eq. (84) for an opacity of $\kappa_{\text{MeV}} \simeq 0.06 \text{ cm}^2 \text{ g}^{-1}$ for MeV photons. The second term in the total heating rate, L_{sh} , comes from the emission from the shock-heated regions which is assumed to closely track the accretion power

$$L_{\text{sh}}(t') = \epsilon_{\text{rad}} L(t')$$

with a radiative efficiency of $\epsilon_{\text{rad}} \leq 1$.

To construct a simple model, we consider the *orbit-averaged* accretion power

$$L(t') = \epsilon \dot{M}_{\text{P}} c^2, \quad \dot{M}_{\text{P}}(t') = \Delta M_{\text{cap}}(t')/P_{\text{orb}}, \quad (90)$$

where ϵ is the accretion efficiency, $P_{\text{orb}} = 10 \text{ d}$ is the orbital period, $\Delta M_{\text{cap}}(t')$ is the per-orbit mass capture at pericenter passage time t' , and \dot{M}_{P} is the orbit-averaged mass-capture rate. This form of the accretion power is a very crude approximation (especially at early times), as it does not take into account the discreteness of the accretion episodes that lead to periodic modulation of the lightcurve. We take the radiative efficiency of the disk outflow to be in the following form

$$\epsilon_{\text{rad}} = \frac{\dot{M}_{\text{P}}/\dot{M}_{\text{P,cr}}}{1 + \dot{M}_{\text{P}}/\dot{M}_{\text{P,cr}}}, \quad (91)$$

where $\dot{M}_{\text{P,cr}} \simeq 10^{-3} M_{\odot} \text{ yr}^{-1} \approx 3 \times 10^{-5} M_{\odot}/10 \text{ d}$ is a critical orbit-averaged accretion rate above which the radiative efficiency of internal shocks approaches unity (below $\dot{M}_{\text{P,cr}}$, the inverse-Compton cooling becomes less efficient, see §5).

⁶ The factor of 0.3 is for the case of a uniform ejecta and it only depends weakly on the density profile (Arnett 1982).

6. APPLICATION TO SN2022JLI

The peculiar transient SN2022jli was initially spectroscopically classified as a Type Ic supernova from the nearby host galaxy NGC 157 at a distance⁷ of $\sim 22 \text{ Mpc}$. The late-time properties of this source are summarized as follows (Moore et al. 2023; Chen et al. 2024; Cartier et al. 2024):

- (i) During the decline phase of normal Type Ic evolution, the optical/near-infrared emission unexpectedly rebrightened and reached a second peak with maximum luminosity of $L \sim 10^{42.5} \text{ erg s}^{-1}$ around 50 days since discovery (or roughly 60 days after the inferred explosion time). After a long, gradual decline, the optical and near-infrared luminosities abruptly dropped by more than one order of magnitude around 270 days since discovery. This lightcurve behavior requires an additional power source (other than radioactive decay) that turned on with a delay of 1 to 2 months after the explosion and then switched off about 200 days later.
- (ii) When the additional power source is on, both the bolometric and monochromatic (g, r, i, c, o, z bands) lightcurves show coherent modulations at a period of $P \simeq 12.4 \text{ d}$. The phase-folded lightcurves show a fast-rise and gradual-decline profile, which indicates rapid onset of the energy injection and relatively slow release of the injected energy. The rapid onset timescale of $\Delta t \sim 3 \text{ d}$ constrains the physical size of the power source to be $< c\Delta t \sim 10^{16} \text{ cm}$ (for a non-relativistic source). Comparing this with the characteristic radius of the supernova ejecta $R_{\text{ej}} \sim v_{\text{ej}} t \sim 10^{16} \text{ cm} (v_{\text{ej}}/10^9 \text{ cm s}^{-1})(t/100 \text{ d})$, one infers that the extra power source is embedded inside the ejecta.
- (iii) During the second lightcurve peak, a narrow hydrogen $\text{H}\alpha$ emission line is detected and the temporal variations in the blueshift/redshift (with full-width half-maximum $\Delta v_{\text{FWHM}} \sim 1000 \text{ km s}^{-1}$) of the $\text{H}\alpha$ line center follow the same period as in the lightcurve variability. The $\text{H}\alpha$ line luminosity stayed roughly 0.4% of the optical/near-infrared pseudo-bolometric luminosity and it had temporal variations consistent with the periodic modulation of the continuum emission. This shows that the narrow $\text{H}\alpha$ line is causally connected to the extra power source. For instance, the line emitting gas is likely photoionized by the radiation from the extra power source⁸. The rapid line profile variability also indicates that the hydrogen gas is embedded inside the (hydrogen-poor) ejecta.
- (iv) Temporally and spatially coincident high-energy emission in the 1–3 GeV band is detected in a single 2-month time bin between 180 d and 240 d post discovery. The averaged γ -ray luminosity in this time window is $L_{1-3 \text{ GeV}} \simeq 10^{41.5} \text{ erg s}^{-1}$, which is a fac-

⁷ The distance to SN2022jli may be as low as 12 Mpc (Chen et al. 2024), which will make all luminosities lower than the values quoted in this paper by a factor of 3.

⁸ This is supported by the disappearance of the permitted narrow OI emission lines after the shutoff of the extra power source.

TABLE 1
COMPARISON BETWEEN POSSIBLE THEORIES FOR THE EXTRA POWER SOURCE IN SN2022JLI.

observations\theories	CSM interaction	fallback accretion	magnetar	companion accretion
periodicity	X	X	X	✓
embedded power source	nearby CSM?	✓	✓	✓
delayed onset ($t \sim 50$ d)	✓	X	changing μ_B ?	✓
rapid shutoff ($t \sim 270$ d)	✓	fallback rate cutoff?	X	✓
GeV emission	✓	✓	✓	✓
H α line	H-rich CSM?	X	evaporating companion?	✓

tor of ~ 2 less than the contemporary optical/near-infrared luminosity. This shows that a significant fraction of the energy in the power source is channeled into non-thermal particles. Moreover, the 12.4-day phase-folded photon arrival times are significantly clustered near the fast-rise segment of the time window (with $\Delta t \sim 3$ d) and the GeV emission may to be periodically modulated at the statistical significance of 2–3 σ level (limited by the small number of photons).

A number of theories have been considered by the original authors, including (i) interaction between the supernova ejecta with circum-stellar medium (CSM), (ii) accretion of marginally bound fallback material by the compact object, (iii) magnetic dipole spindown of the newborn magnetar (strongly magnetized neutron star), and (iv) accretion from a shock-inflated companion star. In Table 1, we list the pros and cons of these models. Here, “✓” means that the model prediction is consistent with the observed property, “X” means inconsistency, and “?” (with possible reasons) means the model can potentially work under special conditions.

Recently, King & Lasota (2024) proposed a model that is similar to Roche-lobe overflow in ultra-luminous X-ray sources (but with extreme beaming), and they also considered the orbital evolution of the system. Here, for simplicity, we put their model in the (iv) category in Table 1, but they did not consider the expansion of the companion star’s outer envelope. Another model proposed by Zhu et al. (2024) is based on the gradual evaporation of the companion star by the magnetar’s spindown-powered wind and, in their model, a massive hydrogen-rich evaporation flow caused the delayed release of the spindown energy due to a longer photon diffusion timescale. For simplicity, we put their model in the (iii) category in Table 1 because accretion is not considered. Another possibility for the delayed emission is that the magnetic dipole moment μ_B may gradually increase on a timescale of one to two months (Chugai & Utrobin 2022). However, it is difficult for a model based on the spindown power to reproduce the periodicity in the lightcurve of SN2022jli. The same difficulty applies to the fallback accretion scenario.

We note that CSM interaction can produce shocks that are embedded within the supernova ejecta, as long as part of an equatorial concentrated CSM is located sufficiently close to the exploding star (see e.g., Fig. 2 of Smith 2017). To reproduce the delayed onset of the energy injection, the inner edge of the CSM is located at $v_{ej}t_{begin} \sim 3 \times 10^{15}$ cm ($v_{ej}/10^9$ cm s $^{-1}$)($t_{begin}/30$ d). For

the interaction to last for a duration of $t_{end} \sim 270$ d (before the rapid shutoff), a fraction of the CSM gas needs to be located at a distance of $v_{ej}t_{end} \sim 2 \times 10^{16}$ cm ($v_{ej}/10^9$ cm s $^{-1}$)($t_{end}/270$ d). A potential difficulty of the extended hydrogen-rich CSM is that photoionization by the supernova emission may produce narrow H α lines that are not detected in the early time spectra. A more serious difficulty of the CSM-interaction picture lies on the nearly constant period in the observed lightcurve. Even if the CSM has a spatially periodic structure (i.e., the density is a periodic function of radius), a time-dependent outflow speed can easily destroy the periodicity in the shock power.

In the following, we show that the model based on accretion from the shock-inflated companion star can reproduce the main properties of SN2022jli (§6.1–6.4).

6.1. Periodicity and orbital constraints

In this model, the periodic modulation in the lightcurve is due to orbital motion. Here, we consider the orbit of the system before and after the supernova. The post-supernova semimajor axis is given by

$$a = \left[G(M_{ns} + M_*) \left(\frac{P_{orb}}{2\pi} \right)^2 \right]^{1/3} \quad (92)$$

$$\approx 36R_{\odot} \left(\frac{M_{ns} + M_*}{4M_{\odot}} \right)^{1/3} \left(\frac{P_{orb}}{12.4 \text{ d}} \right)^{2/3},$$

where we have ignored the small mass loss from the companion star.

The total binary mass before the supernova is

$$M_{tot} = M_{ns} + M_* + M_{ej}, \quad (93)$$

where M_{ej} is the ejecta mass. We ignore the small difference between the baryonic and gravitational masses of the neutron star. For a pre-supernova circular orbit with semi-major axis a_0 , the relative (orbital) velocity between the two stars is

$$v_{orb,0} = \sqrt{G(M_{ns} + M_* + M_{ej})/a_0}. \quad (94)$$

Let us adopt a coordinate system where the pre-supernova orbit is in the xy plane. We ignore the small momentum deposition on the companion star by the supernova ejecta (see Hirai et al. 2018, for a thorough discussion). In the instantaneous comoving frame of the companion star, the supernova progenitor star is located at $a_0\hat{x}$ and is moving in the \hat{y} direction with velocity $\vec{v}_{orb,0} = v_{orb,0}\hat{y}$. After the supernova, the neutron star

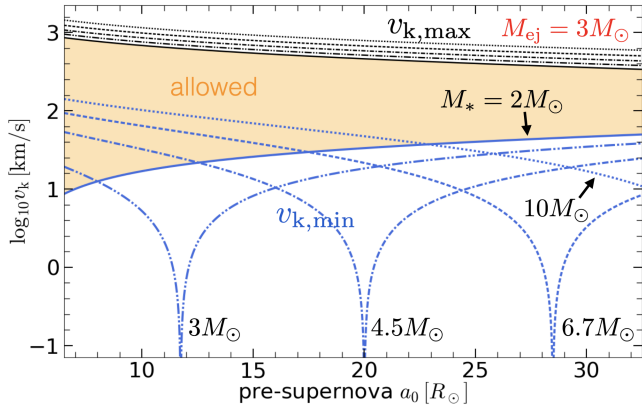


FIG. 16.— Constraints on the magnitude of the natal kick $v_{k,\min} < v_k < v_{k,\max}$. The thin black lines are for the maximum kicks $v_{k,\max}$ and the thick blue lines are for the minimum $v_{k,\min}$. For each companion star mass M_* and pre-supernova separation a_0 , the allowed v_k lies in between the two limits. We marked the allowed region for the $M_* = 3M_\odot$ case in orange and the allowed region is different for other M_* . The ejecta mass is fixed to be $M_{ej} = 3M_\odot$ for all cases, but other ejecta masses $1 \lesssim M_{ej} \lesssim 10M_\odot$ give qualitatively similar results.

receives a natal kick which is denoted as \vec{v}_k , so the total specific energy (per reduced mass) of the post-supernova orbit is given by

$$E_{\text{orb}} = (\vec{v}_{\text{orb},0} + \vec{v}_k)^2/2 - G(M_{\text{ns}} + M_*)/a_0. \quad (95)$$

If $E_{\text{orb}} < 0$, then the binary stays bound with a new semimajor axis a that is given by

$$E_{\text{orb}} = -\frac{G(M_{\text{ns}} + M_*)}{2a}, \quad (96)$$

and the post-supernova orbital period P is related to a by eq. (92). Regardless of the boundness of the orbit, the pericenter separation is given by (a may be negative in this expression if $E_{\text{orb}} > 0$)

$$r_p = a \left(1 - \sqrt{1 - \frac{\ell^2}{(M_{\text{ns}} + M_*)a}} \right), \quad (97)$$

where the specific angular momentum (per reduced mass) is given by

$$\vec{\ell} = a_0 \hat{x} \times (v_{\text{orb},0} \hat{y} + \vec{v}_k). \quad (98)$$

For the unbound cases, there is a 50% chance that the neutron star actually reaches the orbital pericenter. If the post-supernova total velocity is pointing away from the companion star, the neutron star will not reach the pericenter (in such cases, the closest separation between the NS and the companion star is a_0). Generally, we have the following constraint on the post-supernova orbit:

$$r_p \leq a_0. \quad (99)$$

The magnitude of the natal kick may be constrained by the post-supernova orbital period $P_{\text{orb}} = 12.4$ d. For a given kick magnitude $v_k = |\vec{v}_k|$, P is the longest (or shortest) when \vec{v}_k is aligned (anti-aligned) with $\vec{v}_{\text{orb},0}$. Thus, for a known orbital period, we obtain a lower limit

and an upper limit for the kick amplitude

$$v_{k,\min} = \left| \sqrt{G(M_{\text{ns}} + M_*)(2/a_0 - 1/a)} - v_{\text{orb},0} \right|, \quad (100)$$

$$v_{k,\max} = \sqrt{G(M_{\text{ns}} + M_*)(2/a_0 - 1/a)} + v_{\text{orb},0}.$$

These limits are shown in Fig. 16. Unfortunately, we only find weak constraints on the kick amplitude: the region with $100 \lesssim v_k \lesssim 500 \text{ km s}^{-1}$ is generally allowed, for any companion star masses in between 1 and $10 M_\odot$. Although $v_{k,\min}$ may be as low as zero for a particular combination of M_{ej} , M_* and a_0 , we believe this to be a fine-tuned condition. Instead, a finite, minimum kick is statistically required, but the constraint is rather weak ($v_{k,\min} \gtrsim 10 \text{ km s}^{-1}$). We conclude that a wide range of kick velocities between 10 and 500 km s^{-1} may potentially reproduce $P = 12.4$ d. This simply means that it is rather natural to produce a post-supernova orbital period of the order 10 days.

6.2. Delayed onset and rapid shutoff

In our model, the delayed onset of the second peak of the optical lightcurve at $t \sim 50$ d is due to slow expansion of the companion star after the shock impact — this occurs on a timescale of t_{max} (eq. 25). The rapid shutoff of the lightcurve after $t \sim 270$ d is caused by the Kelvin-Helmholtz contraction of the stellar envelope. In this subsection, we use the timing of the delayed onset and rapid shutoff to constrain the pre-supernova orbital separation a_0 , whereas the constraint on the companion star's mass is rather weak.

Since the inflation of the shock-heated companion star takes place on a timescale of t_{max} , which mainly depends on the pre-supernova orbital separation a_0 (eq. 25), we use $50 \lesssim t_{\text{max}} \lesssim 270$ d to constrain a_0 . Based on Fig. 6 (blue shaded region in the upper panel), we obtain the following conservative constraints on a_0 :

$$10 \lesssim a_0 \lesssim 30 R_\odot, \quad (\text{from SN2022jli timing}) \quad (101)$$

which is only very weakly dependent of companion mass. This is consistent with the sufficient condition for accretion (eq. 26), as long as the pre-supernova orbital separation is $a_0 \lesssim 20 R_\odot$.

However, in our simplified lightcurve model (Fig. 15), the onset and shutoff of the accretion-powered second peak are not as sharp as observed.

We speculate that this might be due to the effects of accretion feedback on the structure of the star's outer envelope. At early time when R_* just expands past r_p , the outermost layers of the envelope may be rapidly removed by the mechanical energy output from accretion. This is possible for sufficiently strong ram pressure of the disk outflow $P_w \gtrsim 10^8 \text{ erg/cm}^3$ (eq. 35), which would overwhelm the ram pressure of the envelope gas in the neutron star's frame (eq. 36). It is possible that the accretion onto the neutron star is only strong when the envelope's density at $r = r_p$ exceeds $10^{-7} \text{ g cm}^{-3}$. Modeling the interactions between the disk outflow and the stellar envelope is beyond the scope of this paper.

Another possibility is that when the accretion rate drops below a threshold given by $P = P_{\text{cr}}$ (eq. 57), the propeller wind suddenly disappears and the total power of

the system drops by a factor of ~ 10 (eq. 59). This could potentially give rise to more abrupt onset and cut-off in the accretion power and hence the lightcurve in the second peak. Due to theoretical uncertainties of the propeller wind, we do not discuss this possibility in detail.

6.3. GeV emission

In our model, the GeV emission is produced by pp collisions between the cosmic ray protons accelerated by internal shocks ($r_{\text{sh}} \sim 10^{14}$ cm) and the non-relativistic thermal protons. To explain the observed average luminosity of $L_{1-3\text{GeV}} \sim 3 \times 10^{41}$ erg s $^{-1}$ in the 180–240 d time bin, our model likely requires a combination of a relatively high cosmic ray energy efficiency ($\epsilon_p > 0.1$) and a large per-orbit accretion energy release $\epsilon \Delta M_{\text{cap}} c^2 > 2 \times 10^{48}$ erg. Preliminary hydrodynamic numerical simulations (Cary et al., in prep) indeed suggest that ΔM_{cap} is higher than our estimate of $10^{-4} M_{\odot}$ by a factor of a few to 10, so it is plausible to produce the observed GeV luminosity.

More importantly, the delayed onset of the GeV emission means that GeV photons are absorbed by Bethe-Heitler pair production process at $t \lesssim 150$ d, where the upper limit in the escaping time for GeV photons is conservative considering the poor time resolution of the Fermi-LAT lightcurve. Since the opacity for GeV photons is $\kappa_{\text{GeV}} \simeq 0.03 \text{ cm}^2 \text{ g}^{-1}$, we infer from eq. (84) a relatively large ejecta mass of $M_{\text{ej}} \simeq 3 M_{\odot}$. A potential, independent measurement of the ejecta mass may be obtained from the nebular phase ($t \gtrsim 300$ d) of the lightcurve evolution.

6.4. H α line

A natural prediction of our model is the production of hydrogen recombination lines such as H α due to photo-ionization of the slowest (and densest) parts of the disk wind that has not been shock-heated.

Depending on whether the Strömgen sphere encloses the entire wind, the system may be in one of the two regimes: ionization-limited (where a neutral layer exists) or density-limited (the wind is fully ionized). The maximum ionization rate is given by $\dot{N}_{\text{ion}} \sim \xi L_{\text{sh}} / \mathcal{E}_{\text{ion}} \sim 10^{53} \text{ s}^{-1} L_{\text{sh},43}$, where we have taken a fraction $\xi \sim 0.5$ of the luminosity L_{sh} from internal shocks to be used in ionization and each ionization costs an average amount of energy $\mathcal{E}_{\text{ion}} \sim 30$ eV (the ionization is physically due to Compton-heated electrons colliding with hydrogen atoms). The maximum mass of the ionized gas is

$$M_{\text{ion,max}} \sim \frac{\dot{N}_{\text{ion}} m_p}{n \alpha_B} \sim 10^{-2} M_{\odot} \dot{N}_{\text{ion},52} n_{11}^{-1} T_5^{0.7}, \quad (102)$$

where n is the gas number density (eq. 70), $\alpha_B \simeq 2.6 \times 10^{-13} (T/10^4 \text{ K})^{-0.7}$ is the Case-B recombination coefficient, and we have taken $T = 10^5 T_5$ K as a fiducial value for the temperature of the ionized gas. We find $M_{\text{ion,max}} > \Delta M_{\text{cap}}$ to be the typical case, so the system is in the density-limited regime, which leads to a relatively small H α yield $L_{\text{H}\alpha} / L_{\text{sh}} < 1\%$ than the ionization-limited regime. From the H α recombination branching fraction $\alpha_B^{\text{H}\alpha} / \alpha_B \approx 0.3$, we can estimate the H α luminosity by assuming that the entire slow wind of mass ΔM_{cap}

is fully ionized,

$$\begin{aligned} L_{\text{H}\alpha} &\sim n \alpha_B \frac{\Delta M_{\text{cap}}}{m_p} \frac{\alpha_B^{\text{H}\alpha}}{\alpha_B} \mathcal{E}_{\text{H}\alpha} \\ &\sim 10^{39} \text{ erg s}^{-1} n_{11} T_5^{-0.7} \frac{\Delta M_{\text{cap}}}{10^{-4} M_{\odot}}, \end{aligned} \quad (103)$$

where $\mathcal{E}_{\text{H}\alpha} = 1.9$ eV is the H α photon energy. Since the gas density scales as $n \propto \Delta M_{\text{cap}} / r_{\text{sh}}^{-3}$, we find $L_{\text{H}\alpha} \propto \Delta M_{\text{cap}}^2 / r_{\text{sh}}^{-3}$. The observed H α luminosity reaches up to 5×10^{39} erg s $^{-1}$ (and possibly even higher near the 2nd peak of the optical lightcurve), which can be produced if the Bondi-captured mass per orbit is $\Delta M_{\text{cap}} \gtrsim 3 \times 10^{-4} M_{\odot}$.

Another piece of information is the H α line profile, which is observed to undergo rapid variations of the Doppler shift on the orbital timescale. The peak of the line has velocities of the order 10^3 km s $^{-1}$, but the width may extend to larger velocities up to 5000 km s $^{-1}$. These velocities are consistent with our model where the H-rich disk outflow has a wide range of velocities and most of the mass is contained in the slowest outflow components near 10^3 km s $^{-1}$ that dominates the H α luminosity.

7. SUMMARY

In this work, we study the aftermath of the interaction between the ejecta of a stripped-envelope supernova and a close-by main-sequence companion star, motivated by the recent observations of the peculiar Type Ic supernova SN2022jli (Moore et al. 2023; Chen et al. 2024; Cartier et al. 2024).

We first construct a 1D model for the shock-heated stellar envelope by entropy injection according to the Rankine-Hugoniot jump condition. Then, we use MESA to follow the subsequent evolution of the ejecta-impacted star. It is found that the stellar envelope gradually expands to a maximum radius R_{max} up to $\sim 10^2 R_{\odot}$ (eq. 24) that is mainly dependent on the pre-supernova separation a_0 . If the neutron star remains in a bound orbit, the pericenter radius r_p is constrained to be $r_p \leq a_0$. Thus, a sufficient condition for neutron star accretion from the stellar envelope is given by $R_{\text{max}}(a_0) > a_0$, which is shown to correspond to $a_0 \lesssim 20 R_{\odot}$ (nearly independent of the companion star's mass) or pre-supernova orbital period $P_0 \lesssim 3 \text{ d} (M_{\text{tot}}/10 M_{\odot})^{-1/2}$ for a total mass of M_{tot} . Neutron star accretion may also occur for wider pre-supernova orbits for favorable orientations of the natal kick.

The time it takes for the ejecta-impacted companion star to expand to the maximum radius also mainly depends on a_0 as $t_{\text{max}} \sim 290 \text{ d} (a_0/10 R_{\odot})^{-12/5}$ (eq. 25). The slow expansion of the stellar envelope leads to a delayed onset of the neutron star accretion, which may cause the supernova optical lightcurve to be double-peaked, as the onset of the accretion power is usually delayed by more than the peak time of Type Ib/c supernovae (~ 10 d). At late time $t > t_{\text{max}}$, the outer envelope undergoes Kelvin-Helmholtz contraction, and this causes the accretion power to disappear, so the supernova emission returns to the normal nebular phase.

We then study the accretion power from the gravitationally captured gas, taking into account the interactions between the accretion disk and the neutron star magnetosphere. We find that, for $a_0 \lesssim 20 R_\odot$, the typical mass capture per orbit is $\Delta M_{\text{cap}} \gtrsim 10^{-4} M_\odot$ near the maximum stellar radius ($R_* \sim R_{\text{max}}$). The disk has a high accretion rate of the order $\dot{M}_d \sim 0.1 M_\odot/\text{yr}$, and a powerful disk wind may be produced from near the Alfvén radius where the disk is truncated by the neutron star magnetospheric pressure. We find that an accretion efficiency of the order $\epsilon = \Delta E / (\Delta M_{\text{cap}} c^2) \sim 10^{-2}$ is possible when the system is in the “propeller” state for a typical Crab-like neutron star. Thus, each accretion episode produces an energy of the order $\Delta E \sim 10^{48} \text{ erg } \epsilon_{-2} (\Delta M_{\text{cap}} / 10^{-4} M_\odot)$, mostly in the kinetic form.

The disk wind has a wide range of velocities from $v_{\text{min}} \sim 10^3 \text{ km/s}$ to a fraction of speed of light, as the slowest parts (carrying most of the mass ΔM_{cap}) are launched from the outer disk near $r_d \sim 0.3 R_\odot$ (eq. 44) and the fastest parts (carrying most of the energy ΔE) are from the inner disk near the Alfvén radius. A consequence of the velocity stratification is that internal shocks are produced near the characteristic radius $r_{\text{sh}} \sim v_{\text{min}} P \sim 10^{14} \text{ cm}$ for an orbital period of $P \sim 10 \text{ d}$. We find the internal shocks to be radiative, thanks to efficient inverse-Compton cooling. Thus, a large fraction of ΔE will be converted into radiation energy (mostly carried by MeV photons), which will then be reprocessed by the supernova ejecta into the optical band. The unshocked slowest parts of the disk wind are photo-ionized, which produces narrow ($\sim 10^3 \text{ km/s}$) Balmer lines by recombination that would otherwise be highly unusual for Type Ib/c supernovae in terms of the hydrogen composition and linewidth.

We also study the non-thermal emission from the internal shocks. It is found that cosmic ray protons rapidly cool due to hadronic pp collisions, and hence a fraction $\epsilon_p \sim 0.1$ of the outflow energy ΔE is converted into γ -rays and neutrinos — these high-energy messengers have energies ranging from 100 MeV up to 10 PeV, but most of their energies are carried by $\sim \text{GeV}$ ones that are produced by mildly relativistic cosmic ray protons, with a

typical time-averaged luminosity of $L_{\text{GeV}} \sim 10^{41} \text{ ergs}^{-1}$ (eq. 83) that is comparable between GeV photons and neutrinos. The neutrinos escape without any obscuration, but GeV photons are absorbed by the supernova ejecta in the first $\sim 100 \text{ d}$ (eq. 84) due to Bethe-Heitler pair production. This causes the emerging GeV emission to be delayed compared to the 2nd peak of the optical lightcurve.

Our model provides a self-consistent explanation of the puzzling properties of SN2022jli, including the delayed onset and rapid shutoff of the second peak, periodic modulations, delayed GeV emission, and narrow Balmer lines. The main requirement is that the companion star was at a very close pre-supernova separation of $10 \lesssim a_0 \lesssim 20 R_\odot$ (or orbital period $1 \lesssim P_0 \lesssim 3 \text{ d}$ for a total mass near $10 M_\odot$), which comes from the requirement of $50 \lesssim t_{\text{max}} \lesssim 270 \text{ d}$. Such a tight binary system is most likely formed by common-envelope evolution (as found in population synthesis models, e.g., Ko et al. 2025). Unfortunately, our model does not provide a strong constraint on the mass of the companion star. It may be possible to constrain the companion mass by directly observing the companion star after the supernova has faded away. A comparison between Figs. 4 and 5 suggests that a higher mass companion star would appear like a blue supergiant for a longer duration. For instance, a star with $L_* \sim 10^5 L_\odot$ and $T_{\text{eff}} \simeq 10^4 \text{ K}$ would have an AB magnitude of 24-25 mag in the optical bands at a distance of 22 Mpc. However, detecting such a star would require difference imaging with high angular resolution.

Our model motivates detailed hydrodynamic simulations of the interactions between a newly born neutron star and a shock-inflated companion star, and the internal shocks between adjacent episodes of disk outflows.

ACKNOWLEDGMENT

We thank Ping Chen, J.J. Eldridge, and Raffaella Margutti for useful discussions. The research of W.L. and S.C. is supported by the Hellman Fellows Fund. This research benefited from interactions at workshops funded by the Gordon and Betty Moore Foundation through grant GBMF5076 and through interactions at the Kavli Institute for Theoretical Physics, supported by NSF PHY-2309135. D.T. is supported by the Sherman Fairchild Postdoctoral Fellowship at Caltech.

REFERENCES

- Aartsen M. G., et al., 2017, *Journal of Instrumentation*, **12**, P03012
- Arnett W. D., 1982, *ApJ*, **253**, 785
- Atwood W. B., et al., 2009, *ApJ*, **697**, 1071
- Basko M. M., Sunyaev R. A., 1976, *MNRAS*, **175**, 395
- Bauer E. B., White C. J., Bildsten L., 2019, *ApJ*, **887**, 68
- Begelman M. C., 1979, *MNRAS*, **187**, 237
- Blandford R. D., Begelman M. C., 1999, *MNRAS*, **303**, L1
- Cartier R., et al., 2024, *arXiv e-prints*, p. arXiv:2410.21381
- Cary S., Lu W., Leung C., Wong T. L. S., 2025, *arXiv e-prints*, p. arXiv:2507.10682
- Chatzopoulos E., Wheeler J. C., Vinko J., Horvath Z. L., Nagy A., 2013, *ApJ*, **773**, 76
- Chen H.-P., Rau S.-J., Pan K.-C., 2023, *ApJ*, **949**, 121
- Chen P., et al., 2024, *Nature*, **625**, 253
- Cho H., Prather B. S., Narayan R., Natarajan P., Su K.-Y., Ricarte A., Chatterjee K., 2023, *ApJL*, **959**, L22
- Chugai N. N., Utrobin V. P., 2022, *MNRAS*, **512**, L71
- Crumley P., Caprioli D., Markoff S., Spitkovsky A., 2019, *MNRAS*, **485**, 5105
- Davidson K., Ostriker J. P., 1973, *ApJ*, **179**, 585
- De S., MacLeod M., Everson R. W., Antoni A., Mandel I., Ramirez-Ruiz E., 2020, *ApJ*, **897**, 130
- Dessart L., Audit E., Hillier D. J., 2015a, *MNRAS*, **449**, 4304
- Dessart L., Hillier D. J., Woosley S., Livne E., Waldman R., Yoon S.-C., Langer N., 2015b, *MNRAS*, **453**, 2189
- Dessart L., Yoon S.-C., Aguilera-Dena D. R., Langer N., 2020, *A&A*, **642**, A106
- Dexter J., Kasen D., 2013, *ApJ*, **772**, 30
- Drout M. R., et al., 2011, *ApJ*, **741**, 97
- Drout M. R., Göteborg Y., Ludwig B. A., Groh J. H., de Mink S. E., O’Grady A. J. G., Smith N., 2023, *Science*, **382**, 1287
- Edgar R., 2004, *New Astronomy Reviews*, **48**, 843
- Ekşi K. Y., Hernquist L., Narayan R., 2005, *ApJL*, **623**, L41
- Eldridge J. J., Maund J. R., 2016, *MNRAS*, **461**, L117
- Eldridge J. J., Izzard R. G., Tout C. A., 2008, *MNRAS*, **384**, 1109
- Eldridge J. J., Fraser M., Smartt S. J., Maund J. R., Crockett R. M., 2013, *MNRAS*, **436**, 774
- Ertl T., Woosley S. E., Sukhbold T., Janka H. T., 2020, *ApJ*, **890**, 51

- Filippenko A. V., 1997, *ARA&A*, **35**, 309
 Folatelli G., et al., 2016, *ApJL*, **825**, L22
 Fox O. D., et al., 2022, *ApJL*, **929**, L15
 Frank J., King A., Raine D. J., 2002, *Accretion Power in Astrophysics: Third Edition*
 Fryxell B. A., Arnett W. D., 1981, *ApJ*, **243**, 994
 Ghosh P., Lamb F. K., 1979, *ApJ*, **234**, 296
 Götzberg Y., et al., 2023, *ApJ*, **959**, 125
 Guo M., Stone J. M., Quataert E., Kim C.-G., 2024, *arXiv e-prints*, p. [arXiv:2405.11711](https://arxiv.org/abs/2405.11711)
 Hillas A. M., 1984, *ARA&A*, **22**, 425
 Hirai R., Podsiadlowski P., 2022, *MNRAS*, **517**, 4544
 Hirai R., Sawai H., Yamada S., 2014, *ApJ*, **792**, 66
 Hirai R., Podsiadlowski P., Yamada S., 2018, *ApJ*, **864**, 119
 Hober O., Bear E., Soker N., 2022, *MNRAS*, **516**, 1846
 Hubbell J. H., Gimm H. A., Øverbø I., 1980, *Journal of Physical and Chemical Reference Data*, **9**, 1023
 Jermyn A. S., et al., 2023, *ApJS*, **265**, 15
 Kamae T., Karlsson N., Mizuno T., Abe T., Koi T., 2006, *ApJ*, **647**, 692
 Kasen D., 2010, *ApJ*, **708**, 1025
 Kasen D., Bildsten L., 2010, *ApJ*, **717**, 245
 Kashiyama K., Quataert E., 2015, *MNRAS*, **451**, 2656
 Kato T. N., Takabe H., 2010, *ApJ*, **721**, 828
 Khatami D., Kasen D., 2023, *arXiv e-prints*, p. [arXiv:2304.03360](https://arxiv.org/abs/2304.03360)
 King A., Lasota J.-P., 2024, *A&A*, **682**, L22
 Ko T., Kinugawa T., Tsuna D., Hirai R., Takei Y., 2025, *arXiv e-prints*, p. [arXiv:2506.00931](https://arxiv.org/abs/2506.00931)
 Kremer K., Lu W., Rodriguez C. L., Lachat M., Rasio F. A., 2019, *ApJ*, **881**, 75
 Kremer K., Lombardi J. C., Lu W., Piro A. L., Rasio F. A., 2022, *ApJ*, **933**, 203
 Laplace E., Götzberg Y., de Mink S. E., Justham S., Farmer R., 2020, *A&A*, **637**, A6
 Li W., et al., 2011, *MNRAS*, **412**, 1441
 Liu Z.-W., Tauris T. M., Röpké F. K., Moriya T. J., Kruckow M., Stancliffe R. J., Izzard R. G., 2015, *A&A*, **584**, A11
 Lovelace R. V. E., Romanova M. M., Bisnovaty-Kogan G. S., 1995, *MNRAS*, **275**, 244
 Ludwig B., Drout M. R., Götzberg Y., Lang D., Laroche A., 2025, *arXiv e-prints*, p. [arXiv:2505.18632](https://arxiv.org/abs/2505.18632)
 Lyman J. D., Bersier D., James P. A., Mazzali P. A., Eldridge J. J., Fraser M., Pian E., 2016, *MNRAS*, **457**, 328
 MacLeod M., Ramirez-Ruiz E., 2015, *ApJ*, **803**, 41
 MacLeod M., Antoni A., Murguía-Berthier A., Macias P., Ramirez-Ruiz E., 2017, *ApJ*, **838**, 56
 Margalit B., Quataert E., Ho A. Y. Q., 2022, *ApJ*, **928**, 122
 Marietta E., Burrows A., Fryxell B., 2000, *ApJS*, **128**, 615
 Maund J. R., Pastorello A., Mattila S., Itagaki K., Boles T., 2016, *ApJ*, **833**, 128
 Metzger B. D., Margalit B., Kasen D., Quataert E., 2015, *MNRAS*, **454**, 3311
 Metzger B. D., Beniamini P., Giannios D., 2018, *ApJ*, **857**, 95
 Miller K. A., Stone J. M., 1997, *ApJ*, **489**, 890
 Moore T., et al., 2023, *ApJL*, **956**, L31
 Mushtukov A. A., Suleimanov V. F., Tsygankov S. S., Poutanen J., 2015, *MNRAS*, **454**, 2539
 Nadyozhin D. K., 1994, *ApJS*, **92**, 527
 Narayan R., Yi I., 1995, *ApJ*, **452**, 710
 Ogata M., Hirai R., Hijikawa K., 2021, *MNRAS*, **505**, 2485
 Pan K.-C., Ricker P. M., Taam R. E., 2012, *ApJ*, **760**, 21
 Parfrey K., Tchekhovskoy A., 2017, *ApJL*, **851**, L34
 Parfrey K., Spitkovsky A., Beloborodov A. M., 2016, *ApJ*, **822**, 33
 Park J., Caprioli D., Spitkovsky A., 2015, *Phys. Rev. Lett.*, **114**, 085003
 Paxton B., Bildsten L., Dotter A., Herwig F., Lesaffre P., Timmes F., 2011, *ApJS*, **192**, 3
 Paxton B., et al., 2013, *ApJS*, **208**, 4
 Paxton B., et al., 2015, *ApJS*, **220**, 15
 Paxton B., et al., 2018, *ApJS*, **234**, 34
 Paxton B., et al., 2019, *ApJS*, **243**, 10
 Perets H. B., Li Z., Lombardi James C. J., Milcarek Stephen R. J., 2016, *ApJ*, **823**, 113
 Piro A. L., Ott C. D., 2011, *ApJ*, **736**, 108
 Podsiadlowski P., Joss P. C., Hsu J. J. L., 1992, *ApJ*, **391**, 246
 Prentice S. J., et al., 2019, *MNRAS*, **485**, 1559
 Rimoldi A., Portegies Zwart S., Rossi E. M., 2016, *Computational Astrophysics and Cosmology*, **3**, 2
 Romanova M. M., Ustyugova G. V., Koldoba A. V., Lovelace R. V. E., 2004, *ApJL*, **616**, L151
 Rybicki G. B., Lightman A. P., 1986, *Radiative Processes in Astrophysics*
 Shakura N. I., Sunyaev R. A., 1973, *A&A*, **24**, 337
 Shivvers I., et al., 2017, *PASP*, **129**, 054201
 Smith N., 2017, in Alsabti A. W., Murdin P., eds., *Handbook of Supernovae*. p. 403, doi:[10.1007/978-3-319-21846-5_38](https://doi.org/10.1007/978-3-319-21846-5_38)
 Smith N., Li W., Filippenko A. V., Chornock R., 2011, *MNRAS*, **412**, 1522
 Spitkovsky A., 2008, *ApJL*, **673**, L39
 Stone J. M., Pringle J. E., 2001, *MNRAS*, **322**, 461
 Stone J. M., Pringle J. E., Begelman M. C., 1999, *MNRAS*, **310**, 1002
 Sun N.-C., Maund J. R., Hirai R., Crowther P. A., Podsiadlowski P., 2020, *MNRAS*, **491**, 6000
 Taddia F., et al., 2015, *A&A*, **574**, A60
 Taddia F., et al., 2018, *A&A*, **609**, A136
 Tauris T. M., Langer N., Podsiadlowski P., 2015, *MNRAS*, **451**, 2123
 Thorne K. S., Zytzkow A. N., 1977, *ApJ*, **212**, 832
 Tsuna D., Lu W., 2025, *ApJ*, **986**, 84
 Tsuna D., Takei Y., 2023, *PASJ*, **75**, L19
 Van Dyk S. D., de Mink S. E., Zapartas E., 2016, *ApJ*, **818**, 75
 Verner D. A., Ferland G. J., Korista K. T., Yakovlev D. G., 1996, *ApJ*, **465**, 487
 Wang Y. M., 1995, *ApJL*, **449**, L153
 Wheeler J. C., Lecar M., McKee C. F., 1975, *ApJ*, **200**, 145
 Wheeler J. C., Johnson V., Clocchiatti A., 2015, *MNRAS*, **450**, 1295
 White C. J., Quataert E., Gammie C. F., 2020, *ApJ*, **891**, 63
 Woosley S. E., 2010, *ApJL*, **719**, L204
 Woosley S. E., 2019, *ApJ*, **878**, 49
 Woosley S. E., Langer N., Weaver T. A., 1995, *ApJ*, **448**, 315
 Woosley S. E., Sukhbold T., Kasen D. N., 2021, *ApJ*, **913**, 145
 Yoon S.-C., 2015, *PASA*, **32**, e015
 Yuan F., Wu M., Bu D., 2012, *ApJ*, **761**, 129
 Yuan F., Gan Z., Narayan R., Sadowski A., Bu D., Bai X.-N., 2015, *ApJ*, **804**, 101
 Zapartas E., et al., 2017, *ApJ*, **842**, 125
 Zhu J.-P., Liu L.-D., Yu Y.-W., Mandel I., Hirai R., Zhang B., Chen A., 2024, *ApJL*, **970**, L42
 de Jager O. C., Harding A. K., Michelson P. F., Nel H. I., Nolan P. L., Sreekumar P., Thompson D. J., 1996, *ApJ*, **457**, 253

physics \LaTeX template. The OJA is a journal which provides fast and easy peer review for new papers in the `astro-ph` section of the arXiv, making the reviewing process simpler for authors and referees alike. Learn more at <http://astro.theoj.org>.

APPENDIX

In this appendix, we show Fig. 17 which demonstrates that our results are insensitive to the choices of envelope heating time Δt (eq. 18) and minimum exterior mass $m_{\text{ex,min}}$ (eq. 20).

This paper was built using the Open Journal of Astro-

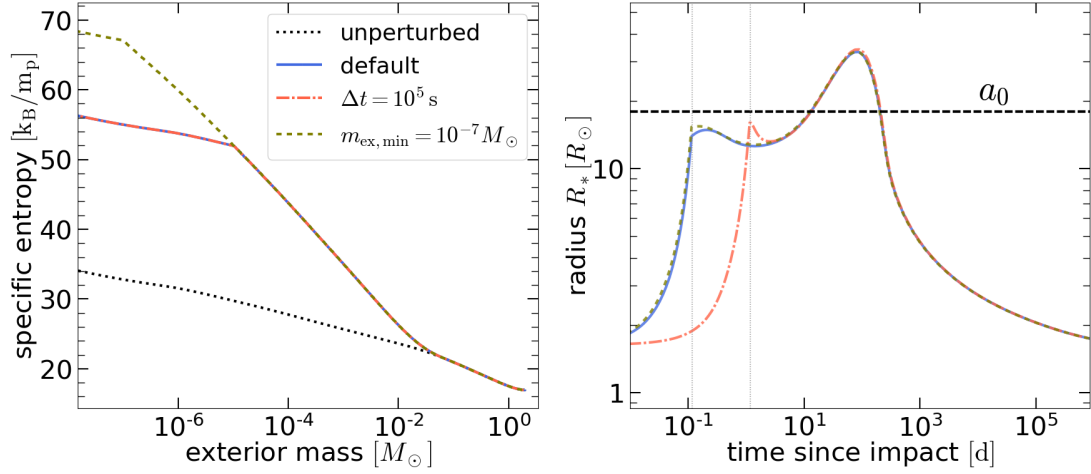


FIG. 17.— The left panel shows the entropy profiles before (black dotted) and after (colored lines) shock heating. The right panel shows the radius evolution of the star in different cases. The default case (blue solid line) has heating time $\Delta t = 10^4$ s and minimum exterior mass $m_{\text{ex,min}} = 10^{-5} M_{\odot}$ below which the entropy jump is taken to be flat. Two other cases are considered: one with $\Delta t = 10^5$ s (red dash-dotted line) and the other one (green dashed line) with $m_{\text{ex,min}} = 10^{-7} M_{\odot}$. For all cases, we take $E_{\text{ej}} = 10^{51}$ erg, $M_* = 2M_{\odot}$, and pre-supernova separation $a_0 = 18R_{\odot}$.